INSTABILITIES OF OVERTURNED TRAVELING WAVES

DISSERTATION

Tyler B. Pierce, Maj, USAF
AFIT/ENC

DEPARTMENT OF THE AIR FORCE
AIR UNIVERSITY

AIR FORCE INSTITUTE OF TECHNOLOGY

Wright-Patterson Air Force Base, Ohio

AFIT/ENC

INSTABILITIES OF OVERTURNED TRAVELING WAVES

DISSERTATION

Presented to the Faculty

Graduate School of Engineering and Management

Air Force Institute of Technology

Air University

Air Education and Training Command

in Partial Fulfillment of the Requirements for the

Degree of PhD in Applied Mathematics

Tyler B. Pierce, B.S.Ch.E., M.B.A., M.S.O.R.

Maj, USAF

10 July 2020

AFIT/ENC

INSTABILITIES OF OVERTURNED TRAVELING WAVES

DISSERTATION

Tyler B. Pierce, B.S.Ch.E., M.B.A., M.S.O.R.
Maj, USAF

Committee Membership:

Dr. Benjamin Akers
Chairman

Dr. Mark Oxley
Member

Dr. Dana Morrill
Member

Dr. Tony Liu
Member

Dr. Daniel Emmons
Member, out-of-department

Dr. Raymond Hill
Dean's Representative

Abstract

In this work, we consider the interface between two incompressible, irrotational fluids. Traveling waves, including overturned waves (those which are not functions of the horizontal coordinate), can occur at this interface. The vortex sheet equations [17][33][34] and conformally-mapped Euler equations [42] model this physical phenomenon and have been the subject of numerous studies. With the exception of Crapper waves [47], the stability of overturned waves have not been studied. This dissertation fills this research gap by analyzing the stability of overturned traveling capillary ripples at various Bond numbers using the conformally-mapped Euler equations.

Two separate techniques for computing the spectrum of waves, here referred to as Spectral Stability Analysis (SSA) and Dynamic Stability Analysis (DSA), are presented. These techniques are demonstrated with proof of concept experiments using the pendulum equation and the Akers-Milewski equation. Various techniques for reducing the stiffness of PDEs are also presented. These techniques are demonstrated on the Korteweg-de Vries equation. The SSA and DSA are then used to compute the spectrum of branches of traveling waves in the conformally-mapped Euler equations. Both methods are verified against the known stability of Crapper waves [47]. No super-harmonic instabilities were found for gravity-capillary ripples whose Bond number is less than two. Both methods identified unstable eigenvalues for waves with Bond numbers greater than or equal to two. The results were used to create a 'surface of instability,' the magnitude of the largest unstable eigenvalue for waves whose Bond number is in $[0, 3)$.

Table of Contents

Page

List of Figures

I. Introduction

The study of water waves dates back to Isaac Newton, who made one of the earliest attempts at a theory on the topic [43]. Some of those who contributed to the field include Euler, Laplace, Lagrange, Poisson, Cauchy, Russel, and Stokes. Euler derived the equations of motion for hydrodynamics [27][28][29]. Laplace proposed the first initial value problem with water waves [22]. Lagrange derived linearized equations for small-amplitude waves and solved the system for shallow water [38]. Poisson and Cauchy furthered the development of the initial value problem and assessed waves in deep water [16][15]. Russell performed extensive experiments with waves and made the first recorded observation of a solitary wave [45]. Stokes gave an analysis of waves of finite amplitude and expanded the wave profile with a power series [46]. A more thorough review of the origins of water wave theory is found in [19][20].

Since the origins of water wave theory, extensive work has been done, both analytically and numerically. A review of more recent research pertinent to the current work is found in [26]. This review addresses bifurcation, stability, and the evolution of gravity and capillary-gravity waves.

A fundamental topic of interest in the study of traveling waves is stability. Deconinck and Kutz state, "The investigation of the stability of solutions of a given mathematical model is an essential aspect of understanding the physical system considered. Stability analysis is important for at least three reasons. First, if a physical phenomenon is observable and persists, then the corresponding solution to a valid mathematical model should be stable. Second, if instability is established, the nature

of the unstable modes might hint at what patterns may develop from the unstable solutions. Third, for many problems of physical interest, fundamental mathematical models are well established. However, in many cases these fundamental models are too complicated to allow for detailed analysis, thus leading to the study of simpler approximate models using reductive perturbation methods. Consequently, the stability analysis can be used to validate or to suggest modifications to the mathematical models used for a given application [24]."

Examples of water wave stability analysis include the following. In the 1960's Benjamin and Feir showed analytically that, under a weakly nonlinear assumption, periodic gravity waves on deep water are unstable with respect to long-wave perturbations [11][10]. In the 1970's Longuet-Higgins initiated numerical studies of the spectral stability of deep waves with sub- and super-harmonic perturbations [39][40]. Numerical studies of spectral stability were later extended to water waves in finite depth [31][37]. In 2011, Deconinck and Oliveras used a Fourier-Floquet decomposition technique to estimate the full spectrum of various traveling wave solutions (in shallow water and deep water) [25]. In a series of articles, Akers and Nichols used a 'Transformed Field Expansions' method to simulate the spectrum as a function of the wave amplitude under various conditions [7][5][6][8].

Of particular interest to the work in this dissertation are overturned waves, or waves whose profiles are not a function of the horizontal spatial coordinate. G. D. Crapper developed a closed-form solution for capillary waves of arbitrary amplitude in water of infinite depth. As the wave amplitude increases, the wave becomes steeper, eventually overturning. The amplitude of Crapper waves are limited to 0.730 wavelengths. For larger waves, the interface intersects, enclosing air bubbles in the troughs [21]. Figure 1 shows Crapper's original figure portraying the profile of several Crapper waves. Tiron and Choi have studied the stability of Crapper waves, finding

that they are stable to super-harmonic perturbations but unstable to sub-harmonic perturbations; both results applying to the entire amplitude range [18][32][47].

Some wave models have been shown to have solutions with overturned waves. One such model is the vortex sheet formulation of the water wave problem. A vortex sheet is the interface between two irrotational fluids, where the only vorticity ($\nabla \cdot u = 0$) is at the interface. Traveling waves may form at this interface. The existence of overturned traveling waves in vortex sheets have been shown [3][2][4][41][44]. Milewski, Vanden-Broeck, and Wang developed a water wave model based on a conformal mapping of the Euler equations. Solutions to the conformally-mapped Euler equations include overturned traveling waves [42]. While the existence of overturned traveling waves have been demonstrated with the vortex sheet equations and the conformally-mapped Euler equations, the stability of these waves (except for Crapper waves) have not yet been determined.

The fundamental contribution of this dissertation is numerically computing the spectrum of overturned, traveling, gravity-capillary waves. The spectrum establishes the stability of these waves. Two different techniques are developed here. The first technique will be called 'Spectral Stability Analysis' (SSA). This technique mimics the Fourier-Floquet approach used by Deconinck and Oliveras in which the wave problem is converted into an eigenvalue problem. It is then solved in Fourier space, giving the full spectrum of the wave in the limit as the number of Fourier modes goes to infinity [25].

The second technique will be called 'Dynamic Stability Analysis' (DSA). In this technique, a solution is perturbed then evolved numerically with a time-stepping algorithm. If the wave is unstable, then a lower bound for the real part of the largest positive eigenvalue is recoverable from the data.

In this dissertation, both of these techniques are demonstrated on two systems

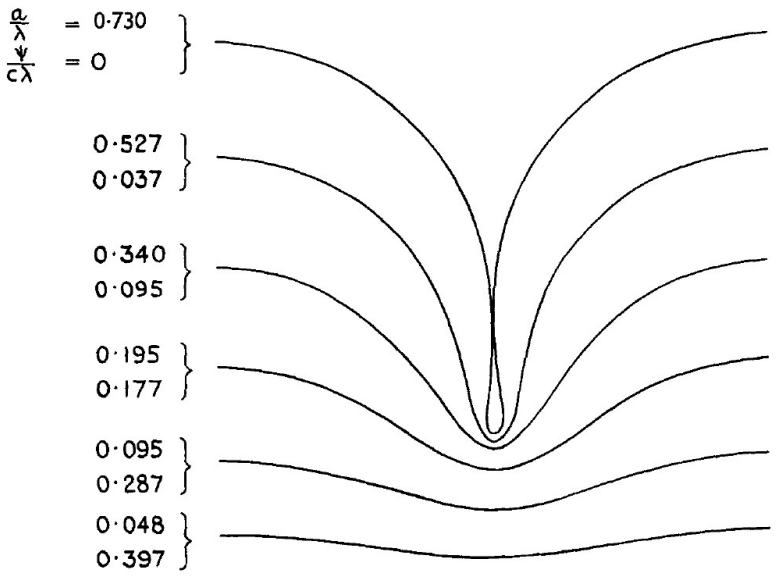

Figure 1. Profile of Crapper Waves. The values on the left give the parameters for the adjacent wave, where a is the amplitude, λ is the wavelength, ψ is the stream function, and c is the wave speed.

whose stabilities are already established. The first system is a simple pendulum. The second system is the Akers-Milewski equation. These demonstrations are used as a proof of concept for SSA and DSA. The techniques are then applied to the vortex sheet equations and the conformally-mapped Euler equations.

An additional topic woven throughout is PDE stiffness. The linear spectrum of some PDEs leads to stiff dynamics. This makes numerical time-stepping algorithms computationally expensive. Several techniques have been developed to reduce this problem. Kassam and Trefethen give a comparison of various techniques [36]. These techniques include, but are not limited to, integrating factors, splitting schemes, and implicit-explicit (IMEX) schemes [9]. In this work, integrating factors are used with the Akers-Milewski equation. Additionally, all three techniques are explored with the Korteweg-de Vries equation. The method of integrating factors was implemented with the vortex sheet equations and the conformally-mapped Euler equations. However, in both instances, it resulted in poor performance. Due to the complexity of these

models, there is a high likelihood that an error was made during the derivation and/or implementation. This leaves an area for additional work.

Stability analysis of overturned traveling water waves does not have direct military application. However, the demonstrated techniques can be adapted to other dynamical systems whose application is military-centric. An example is lasers, whose propagation is characterized by waves.

II. Background

This section begins with a basic overview of dynamical systems. Then, a handful of experiments are presented to develop and demonstrate a general approach to characterizing instabilities of equilibria of dynamical systems and traveling waves. It begins with an analysis of a simple pendulum. Then, the stability of traveling waves associated with the Akers-Milewski (AM) equation are assessed and stiffness reduction techniques are demonstrated on the Korteweg-de Vries (KdV) equation. Finally, the vortex sheet equations and conformally-mapped Euler equations are presented.

2.1 Dynamical Systems

Dynamical systems are those in which mathematical formulas are used to characterize a physical phenomenon whose state changes with time [23]. Dynamical systems are often modeled with differential equations. For example,

$$\mathbf{x}_t = F(\mathbf{x}) \tag{1}$$

where $\mathbf{x}_t$ is the derivative of function $\mathbf{x}$ with respect to time, t (i.e., $\mathbf{x}_t = \frac{d\mathbf{x}}{dt}$).

When possible, analytical solutions allow a user to identify the state of the system at any point in time. However, many differential equations are too complex to solve analytically. In these cases, numerical methods can be used to sequentially step forward in time, solving for the system state at each iteration.

2.2 Pendulum

The pendulum is a simple physical apparatus that can be modeled to demonstrate the concepts of dynamical systems. In Figure 2, a bob is connected to a pivot point

via a stiff, weightless rod. The bob is allowed to swing 360^o around the pivot point. If damping effects are ignored, then the equation governing the pendulum is given by Equation 2 [12].

$$\theta_{tt} + \frac{g}{L}\sin(\theta) = 0 \tag{2}$$

where θ is the angular displacement from the downward vertical position, g is the gravitational constant, and L is the length of the rod. To simplify the presentation, assume that $L = g$. Therefore,

$$\theta_{tt} + \sin(\theta) = 0. \tag{3}$$

In order to get Equation 2 into the form of Equation 1, define $\mathbf{x} = \left[\begin{smallmatrix} x_1 \\ x_2 \end{smallmatrix}\right] = \left[\begin{smallmatrix} \theta \\ \theta_t \end{smallmatrix}\right]$. So,

$$\mathbf{x}_t = \begin{bmatrix} x_{1_t} \\ x_{2_t} \end{bmatrix} \begin{bmatrix} x_2 \\ -\sin(x_1) \end{bmatrix} = F(\mathbf{x}) \tag{4}$$

which is in the form of Equation 1.

Equilibrium Points of the Pendulum.

The equilibrium points of the pendulum equation will now be calculated. First, $\mathbf{x}_t$ is set equal to the zero vector to yield,

$$\mathbf{x}_t = \begin{bmatrix} 0 \\ 0 \end{bmatrix} = \begin{bmatrix} x_2 \\ -\sin(x_1) \end{bmatrix}. \tag{5}$$

Solving this system gives $x_1 = n\pi$ and $x_2 = 0$, where $n \in \mathbb{Z}$. Therefore, the bob of the pendulum is at an equilibrium point when it is positioned exactly below the pivot point (i.e., $\theta = 2n\pi$) or above it (i.e., $\theta = 2n\pi + \pi$). See Figure 3. Looking at how the pendulum responds to small perturbations from the equilibrium points

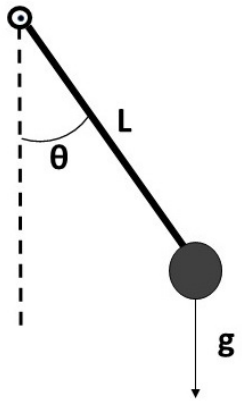

Figure 2. Diagram of a Pendulum.

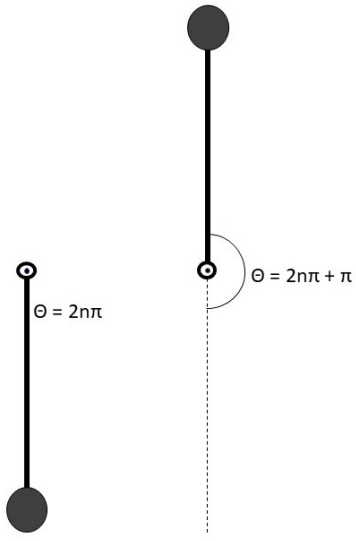

..

Figure 3. Equilibrium Points of a Pendulum.

determines the stability of these points. Intuitively, the equilibrium point that is positioned below the pivot point is stable. In other words, when the bob is slightly perturbed away from this equilibrium point, it will move back toward the equilibrium point and oscillate around it. When damping effects are present, the oscillation will shrink as the bob eventually comes to rest at the equilibrium point. Conversely, the equilibrium point that is positioned above the pivot point is unstable; when slightly perturbed it will move away. The following sections provide the analysis to verify this intuition.

Linear Stability Analysis of the Pendulum.

In order to analytically determine the stability, consider small perturbations of an equilibrium point. Let $\mathbf{x} = \bar{\mathbf{x}} + \delta\,\omega$, where $\bar{\mathbf{x}}$ is an equilibrium point, δ is a small, scalar constant, and ω is a perturbation vector. Substituting this expression into Equation 1 yields

$$(\bar{\mathbf{x}} + \delta\,\omega)_t = F(\bar{\mathbf{x}} + \delta\,\omega) \tag{6}$$

$$\cancelto{0}{\bar{\mathbf{x}}_t} + \delta\,\omega_t = F(\bar{\mathbf{x}} + \delta\,\omega). \tag{7}$$

Generating a Taylor series expansion of the right-hand side and canceling higher order terms gives the following result.

$$\omega_t = J(\bar{\mathbf{x}})\,\omega + O(\delta) \tag{8}$$

where $J(\bar{\mathbf{x}})$ is the Jacobian of $F(\mathbf{x})$ evaluated at the equilibrium points $\bar{\mathbf{x}} = \left[\begin{smallmatrix} n\pi \\ 0 \end{smallmatrix}\right]$. Now, evaluating the Jacobian using the definition of $F(\mathbf{x})$ in Equation 4 gives,

$$J(\mathbf{x}) = \begin{bmatrix} 0 & 1 \\ -\cos(x_1) & 0 \end{bmatrix}. \tag{9}$$

If the $O(\delta)$ term of Equation 8 is ignored, then the resulting equation is a homogeneous linear system of ODEs,

$$\omega_t - J(\bar{\mathbf{x}})\,\omega = 0. \tag{10}$$

Inserting the equilibrium points result in a homogeneous linear system of ODEs with constant coefficients, the solution of which is,

$$\omega_j = \mathbf{v}_j e^{\lambda_j\, t} \tag{11}$$

where $\mathbf{v}_j$ and λ_j are the eigenvectors and eigenvalues of the Jacobian matrix, respectively [13]. The real part of the eigenvalues indicate the stability of the equilibrium point. If there exists λ_j such that $Re(\lambda_j) > 0$, then the equilibrium point is unstable. Conversely, if $Re(\lambda_j) \leqslant 0\ \forall \lambda_j \in \Lambda$, where Λ is the spectrum, then it is stable [14]. The stability of the equilibrium points of the pendulum are calculated next.

Case 1: $\bar{\mathbf{x}}_\mathbf{1} = [2n\pi, 0]^{\mathrm{T}}$ (i.e., the point directly below the pivot point):

Start by calculating the Jacobian matrix,

$$J(\bar{\mathbf{x}}_\mathbf{1}) = \begin{bmatrix} 0 & 1 \\ -\cos(2n\pi) & 0 \end{bmatrix} \tag{12}$$

$$= \begin{bmatrix} 0 & 1 \\ -1 & 0 \end{bmatrix}. \tag{13}$$

Then, calculate the eigenvectors and eigenvalues of the Jacobian matrix,

$$\mathbf{v}_1 = c \begin{bmatrix} -i \\ 1 \end{bmatrix} \tag{14}$$

$$\mathbf{v}_2 = c \begin{bmatrix} i \\ 1 \end{bmatrix} \tag{15}$$

where c is an arbitrary constant. Also,

$$\Lambda(\bar{\mathbf{x}}_\mathbf{1}) = i, -i. \tag{16}$$

Finally, take the real part of the eigenvalues to get

$$Re(\Lambda(\bar{\mathbf{x}}_\mathbf{1})) = [0, 0]^T. \tag{17}$$

Since the eigenvalues are pure imaginary, $\bar{\mathbf{x}}_\mathbf{1}$ is stable. This result confirms the intuition that the equilibrium point just below the pivot point is stable.

Case 2: $\bar{\mathbf{x}}_\mathbf{2} = [2n\pi + \pi, 0]^{\mathrm{T}}$ (i.e., the point directly above the pivot point):

Following the same steps as in Case 1 gives the following result,

$$\mathbf{v}_1 = c \begin{bmatrix} 1 \\ 1 \end{bmatrix} \tag{18}$$

$$\mathbf{v}_2 = c \begin{bmatrix} -1 \\ 1 \end{bmatrix} \tag{19}$$

where c is an arbitrary constant.

$$Re(\Lambda(\bar{\mathbf{x}}_\mathbf{2})) = [1, -1]^T \tag{20}$$

Since $Re(\lambda_j(\bar{\mathbf{x}}_\mathbf{2}))$ are of opposite signs, $\bar{\mathbf{x}}_\mathbf{2}$ is a saddle point, which is unstable. This result confirms the intuition that the equilibrium point directly above the pivot point is unstable.

Dynamic Stability Analysis of the Pendulum.

The pendulum equation is evolved with a fourth order Runge-Kutta time-stepping algorithm. Figure 4 shows the Cauchy error of the first perturbed equilibrium point as a function of the time step, Δt. Since the Runge-Kutta method is fourth order, the Cauchy error should match up to a line with a slope of four on a log-log plot. Therefore, the figure includes lines of slope one, two, three, and four for comparison. In the plot, the Cauchy error data do line up with the fourth order line. The plot reaches a minimum, after which the Cauchy error is fairly flat. This minimum is at or below machine precision. This observation is an indication that the algorithm has been implemented correctly. A similar analysis was made for the other equilibrium point with similar results.

A phase portrait and associated plots provide a qualitative depiction of the stability of the equilibrium points. A few points are selected close to the equilibrium points. These points are evolved through the time-stepping algorithm to determine the trajectories. Figure 5 shows the phase portraits of the pendulum's equilibrium points. Also included are plots of the evolution of the pendulum's angle, θ.

The phase portrait for $\bar{\mathbf{x}}_\mathbf{1} = [0, 0]^T$ shows elliptical trajectories around the equilibrium point. This depiction is indicative of a system whose eigenvalues are pure imaginary [14]. The figure on the right shows that the perturbed point immediately

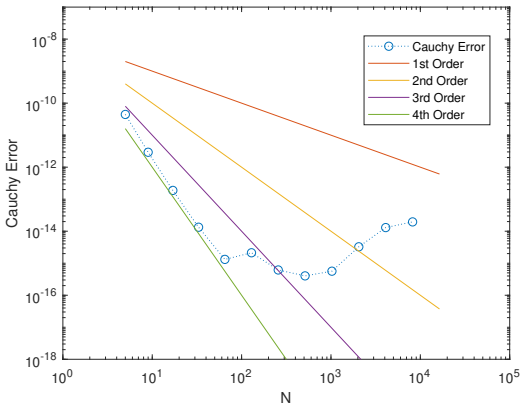

Figure 4. Cauchy Error of Pendulum Equation using RK4. The data indicates that the algorithm is fourth order, as expected for RK4.

begins moving toward the equilibrium point. This trajectory then oscillates around the equilibrium point, as intuition suggests. These observations indicate that the equilibrium point below the pivot point is stable.

The phase portrait for $\bar{\mathbf{x}}_\mathbf{2} = [\pi, 0]^T$ is that of a saddle point. This portrait is indicative of a system with eigenvalues that are both positive and negative [14]. The figure on the right shows that the perturbed point moves away from the equilibrium point. These observations suggest that the equilibrium point above the pivot point is unstable.

Next, the eigenvalues of the pendulum equation are numerically estimated. To do so, let $\mathbf{x_o} = \bar{\mathbf{x}} + \delta\mathbf{v}$, where δ is a small positive constant and $\mathbf{v}$ is a perturbation vector. Then, using a linearization ansatz and ignoring $O(\delta^2)$ terms,

$$\mathbf{x}(t) \approx \bar{\mathbf{x}} + \delta \sum_{j=1}^{2} \alpha_j \mathbf{v}_j e^{\lambda_j t} \tag{21}$$

where α_j are constants, $\mathbf{v}_j$ are eigenfunctions, and λ_j are eigenvalues. Because this is a two-dimensional system, there are only two indices. Rearranging the equation and

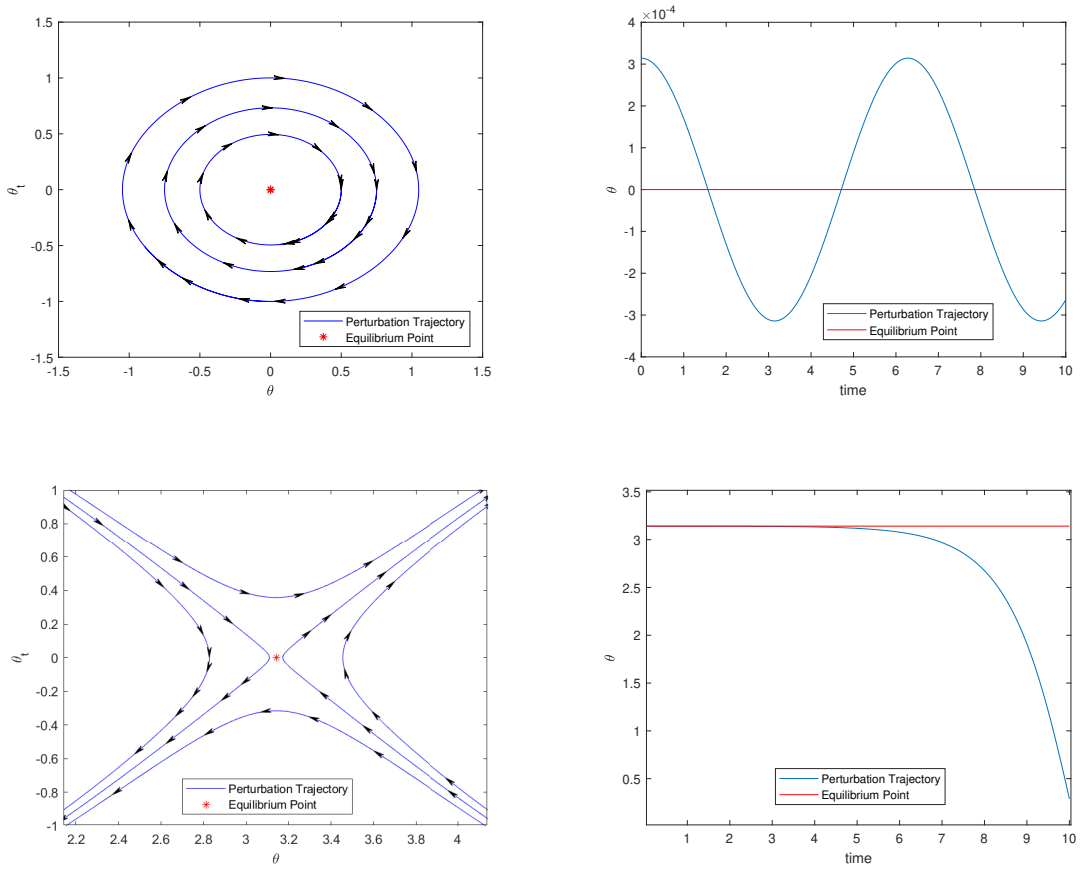

Figure 5. Graphical Stability Evaluation of the Pendulum Equation Near Equilibrium Points. The figures on the left show phase portraits. The figures on the right show the time evolution of θ. The figures on the top are for $\bar{\mathbf{x}}_\mathbf{1} = [0, 0]^T$ and indicate stability at this equilibrium point. The figures on the bottom are for $\bar{\mathbf{x}}_\mathbf{2} = [\pi, 0]^T$ and indicate an unstable equilibrium point.

taking norms gives the following derivation,

$$\mathbf{x}(t) - \bar{\mathbf{x}} \approx \delta \sum_{j=1}^{2} \alpha_j \mathbf{v}_j e^{\lambda_j t} \tag{22}$$

$$\|\mathbf{x}(t) - \bar{\mathbf{x}}\| \approx \delta \| \sum_{j=1}^{2} \alpha_j \mathbf{v}_j e^{\lambda_j t} \|. \tag{23}$$

Using the triangle inequality to take the norm inside the summation yields

$$\|\mathbf{x}(t) - \bar{\mathbf{x}}\| \lesssim \delta \sum_{j=1}^{2} |\alpha_j| \|\mathbf{v}_j\| |e^{\lambda_j t}|. \tag{24}$$

Splitting the eigenvalue into real and imaginary parts yields

$$\|\mathbf{x}(t) - \bar{\mathbf{x}}\| \approx \delta \sum_{j=1}^{2} |\alpha_j| \|\mathbf{v}_j\| |e^{(\mathrm{Re}(\lambda_j) + i\mathrm{Im}(\lambda_j))t}| \tag{25}$$

$$\approx \delta \sum_{j=1}^{2} |\alpha_j| \|\mathbf{v}_j\| e^{\mathrm{Re}(\lambda_j)t} |e^{i\mathrm{Im}(\lambda_j)t}|. \tag{26}$$

Note that $|e^{i\mathrm{Im}(\lambda_j)t}| = 1$, so that

$$\|\mathbf{x}(t) - \bar{\mathbf{x}}\| \approx \delta \sum_{j=1}^{2} |\alpha_j| \|\mathbf{v}_j\| \, e^{\mathrm{Re}(\lambda_j)t}. \tag{27}$$

Multiplying and dividing each index, j, by $e^{Re(\lambda_{max})t}$, where $\mathrm{Re}(\lambda_{max})$ is the eigenvalue with the largest real part yields

$$\|\mathbf{x}(t) - \bar{\mathbf{x}}\| \approx \delta \sum_{j=1}^{2} |\alpha_j| \|\mathbf{v}_j\| e^{\mathrm{Re}(\lambda_{max})t} \left(\frac{e^{\mathrm{Re}(\lambda_j)t}}{e^{\mathrm{Re}(\lambda_{max})t}} \right) \tag{28}$$

$$\approx \delta \sum_{j=1}^{2} |\alpha_j| \|\mathbf{v}_j\| e^{\mathrm{Re}(\lambda_{max})t} \left(\frac{e^{\mathrm{Re}(\lambda_j)}}{e^{\mathrm{Re}(\lambda_{max})}} \right)^t. \tag{29}$$

Note that $\left(\frac{e^{\mathrm{Re}(\lambda_j)}}{e^{\mathrm{Re}(\lambda_{max})}}\right)^t \to 0$ as $t \to \infty$ for $j \neq \max$. Therefore,

$$\|\mathbf{x}(t) - \bar{\mathbf{x}}\| \approx \delta|\alpha_{max}|\|\mathbf{v}_{max}\|e^{\mathrm{Re}(\lambda_{max})t}\cancelto{1}{\left(\frac{e^{\mathrm{Re}(\lambda_{max})}}{e^{\mathrm{Re}(\lambda_{max})}}\right)^t} \tag{30}$$

$$\approx \delta|\alpha_{max}|\|\mathbf{v}_{max}\|e^{\mathrm{Re}(\lambda_{max})t}. \tag{31}$$

Now, take the log of both sides to get

$$\log\|\mathbf{x}(t) - \bar{\mathbf{x}}\| \approx \log\left[\delta e^{\mathrm{Re}(\lambda_{max})t}|\alpha_{max}|\|\mathbf{v}_{max}\|\right] \tag{32}$$

$$\approx \log\left[\delta|\alpha_{max}|\|\mathbf{v}_{max}\|\right] + \log\left[e^{\mathrm{Re}(\lambda_{max})t}\right] \tag{33}$$

$$\approx C + \mathrm{Re}(\lambda_{max})t \tag{34}$$

where $C = \log\left[\delta|\alpha_{max}|\|\mathbf{v}_{max}\|\right]$ is a constant. Therefore, plotting time vs. $\log\|\mathbf{x}(t) - \bar{\mathbf{x}}\|$ should generate a linear relationship, whose slope is $\mathrm{Re}(\lambda_{max})$. It is necessary, however, that the errors, $\|\mathbf{x}(t) - \bar{\mathbf{x}}\|$, remain small relative to the size of δ. Also, when the time-stepping begins, all of the eigenvalues affect the dynamics of the system. It is only when time increases enough, that the affect of λ_{max} dominates that of the other eigenvalues. Therefore, the beginning and end of a plot are to be excluded when determining λ_{max} from the data.

For the initial DSA of the pendulum equation, a perturbation vector of $\mathbf{v} = [1, 0]^T$ is used. Figure 6 shows the time evolution of $\log\|\mathbf{x}(t) - \bar{\mathbf{x}}_\mathbf{1}\|$ for the equilibrium point $\bar{\mathbf{x}}_\mathbf{1} = [0, 0]^T$. However, there does not appear to be a linear portion in the plot. Rather, $\log\|\mathbf{x}(t) - \bar{\mathbf{x}}_\mathbf{1}\| = O(\delta)$, which indicates possible stability at the equilibrium point. From the linear stability analysis, we know this equilibrium point is spectrally stable.

Figure 6 also shows the time evolution of $\log\|\mathbf{x}(t) - \bar{\mathbf{x}}_\mathbf{2}\|$ for the equilibrium point

$\bar{\mathbf{x}}_{\mathbf{2}} = [\pi, 0]^{\mathrm{T}}$. From the plots, it appears that there is a linear relationship within a given time range. A least squares solution of the data in this range provides the $Re(\lambda_{max})$ estimation. As the value of δ approaches zero, the numerical approximation of $Re(\lambda_{max})$ improves (i.e., $\lim_{\delta \to 0} Re(\lambda)(\delta) = Re(\lambda_{max})$). Figure 7 shows $Re(\lambda_{max})$ converging to a value 1.2×10^{-6} less than 1.0, the correct eigenvalue determined previously in the linear stability analysis section.

It should be noted that the perturbation vector, $\mathbf{v} = [1, 0]^{\mathrm{T}}$, used in the above analysis is not equal to the eigenvector, $[1, 1]^{\mathrm{T}}$, determined previously in the linear stability analysis. In order to determine the sensitivity of $Re(\lambda_{max})$ to the perturbation vector, consider a series of perturbation vectors, $\mathbf{v} = [\cos(\theta), \sin(\theta)]^T$ in which θ varies from 0 to 2π. Figure 8 shows $1 - Re(\lambda_{max})$ as a function of θ.

Pendulum Conclusion.

The pendulum was the first dynamical system used as a proof of concept for the research used in this thesis. The equilibrium points were identified as the two points in which the bob of the pendulum is positioned directly below and above the pivot point (i.e., $\bar{\mathbf{x}}_{\mathbf{1}} = [0, 0]^t$ and $\bar{\mathbf{x}}_{\mathbf{2}} = [\pi, 0]^t$). Linear stability analysis identified $\bar{\mathbf{x}}_{\mathbf{1}}$ as stable, with eigenvalues that are purely imaginary. It then identified $\bar{\mathbf{x}}_{\mathbf{2}}$ as unstable, with eigenvalues of ± 1. The Dynamic Stability Analysis identified $\bar{\mathbf{x}}_{\mathbf{1}}$ as possibly stable and $\bar{\mathbf{x}}_{\mathbf{2}}$ as unstable. The accuracy of the maximum eigenvalue estimation depended on the perturbation vector used. The error of the estimated values for $Re(\lambda_{max})$ ranged from 6.2×10^{-6} to 2.1×10^{-9}, depending on the perturbation vector used. Therefore, both SSA and DSA identified $\bar{\mathbf{x}}_{\mathbf{2}}$ as unstable.

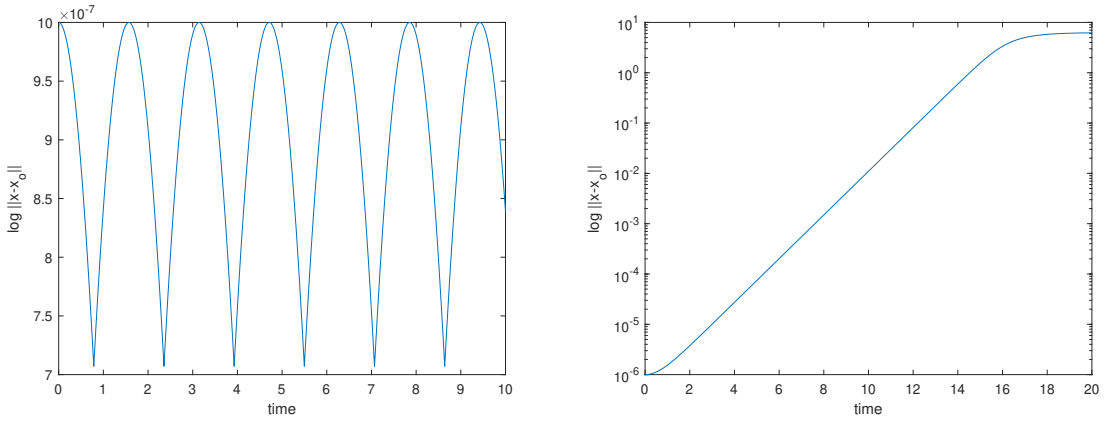

Figure 6. Dynamic Stability Analysis of Pendulum Equation. The figure on the left shows the time evolution of $\log \|\mathbf{x}(t) - \bar{\mathbf{x}}_\mathbf{1}\|$ for the equilibrium point $\bar{\mathbf{x}}_\mathbf{1} = [0, 0]^T$. $\|\mathbf{x}(t) - \bar{\mathbf{x}}_\mathbf{1}\| = O(\delta)$ (i.e., no positive eigenvalues are observed.) The figure on the right shows the time evolution of $\log \|\mathbf{x}(t) - \bar{\mathbf{x}}_\mathbf{2}\|$ for the equilibrium point $\bar{\mathbf{x}}_\mathbf{2} = [\pi, 0]^T$. The slope of the linear portion gives the estimation for $Re(\lambda_{max})$.

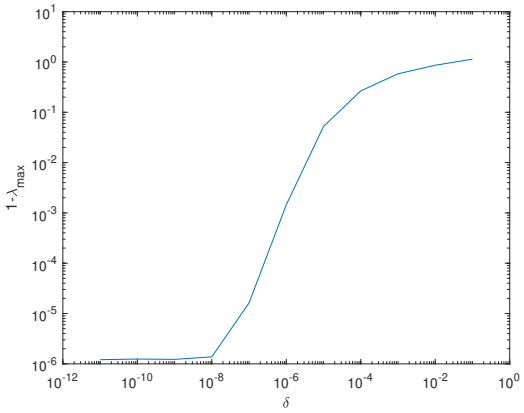

Figure 7. Dynamic Spectral Stability Analysis of Pendulum Equation: Convergence of $Re(\lambda_{max})$. As the perturbation parameter, δ, decreases, the estimation of λ_{max} approaches the correct value of 1.0. The figure shows the data as a difference from the correct value, in log scale.

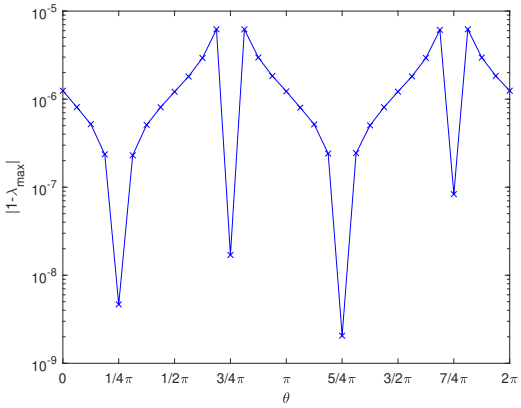

Figure 8. Dependence of Re(λ_{max}) Estimation on Perturbation Vector. The figure shows how Re(λ_{max}) varies as a function of θ when the perturbation vector is defined as $\mathbf{v} = [\cos(\theta), \sin(\theta)]^T$

2.3 Akers-Milewski Equation

The Akers-Milewski equation is a PDE of traveling waves in deep water. Its basic form is

$$u_t - cu_x + \mathscr{H}u - \mathscr{H}u_{xx} - 3/2uu_x = 0 \tag{35}$$

where u represents the height of the wave and $\mathscr{H}$ is the Hilbert transform. Note that this form of the Akers-Milewski equation has the wave represented in a traveling frame of refence. The Hilbert transform [35] is formally defined as

$$\mathscr{H}u(x) = \frac{1}{\pi}\int_{-\infty}^{\infty}\frac{u(\tau)}{x-\tau}d\tau. \tag{36}$$

In frequency domains, the Hilbert transform generates a $-\pi/2$ phase shift. Thus, in Fourier space, the Hilbert transform applied to u becomes $-i\,\mathrm{sign}(k)\hat{u}(k)$.

The Akers-Milewski equation supports depression wave and elevation wave solutions. Figure 9 plots a depression wave solution and an elevation wave solution.

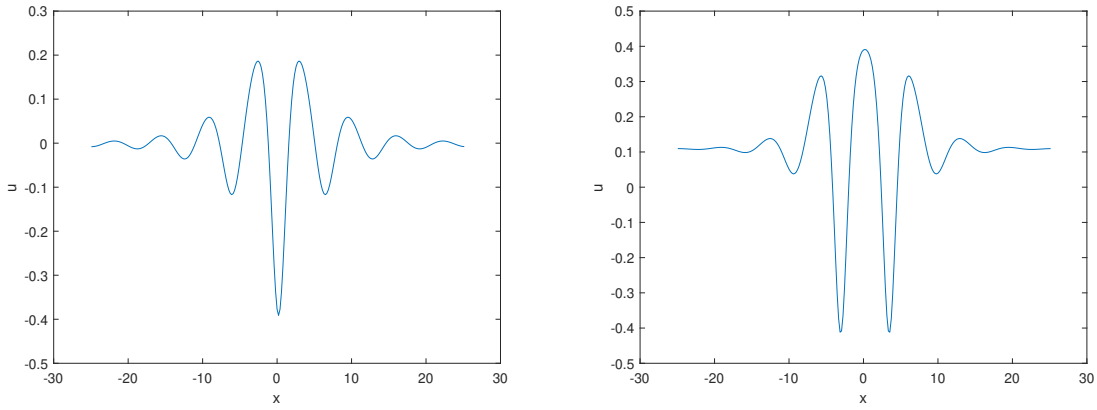

Figure 9. Plots of Solutions to the Akers-Milewski Equation. The figure on the left shows a depression wave (amplitude = -0.4). The figure on the right shows an elevation wave (amplitude = 0.4). NOTE: Amplitude is measured as the distance from a flat surface to the highest/deepest peak/trough.

CFL Condition of the Akers-Milewski Equation.

The CFL condition defines the relationship between the space discretization and the time discretization: $\Delta t \leqslant O(\Delta x^p)$. The CFL condition is based on the numerical method being used and the PDE being solved. The fourth order Runge-Kutta method is the one used in these demonstrations. Most of the time discretization restriction comes from the linear terms of the PDE. Therefore, to estimate the CFL condition, consider the linear portion of the Akers-Milewski equation

$$u_t - cu_x + \mathscr{H}u - \mathscr{H}u_{xx} = 0 \tag{37}$$

with a Fourier space representation of

$$\hat{u}_t = i\left(ck + \text{sign}(k) + \text{sign}(k)k^2\right)\hat{u}. \tag{38}$$

Accordingly, $\lambda = i\left(ck + \text{sign}(k) + \text{sign}(k)k^2\right)$, which is pure imaginary. Next, the stability regions for several Runge-Kutta methods are shown in Figure 10 [1]. The figure shows that the fourth-order method is stable for $-2.9 \leqslant \text{Im}(\lambda\Delta t) \leqslant 2.9$ on the

imaginary axis. Applying this constraint to the Akers-Milewski equation gives the following result,

$$-2.9 \leqslant \mathrm{Im}\big[i(ck + \mathrm{sign}(k) + \mathrm{sign}(k)k^2)\big]\Delta t \leqslant 2.9 \tag{39}$$

$$-2.9 \leqslant O(k^2)\Delta t \leqslant 2.9. \tag{40}$$

Note that $k \leqslant O(N)$. Therefore,

$$-2.9 \leqslant O(N^2)\Delta t \leqslant 2.9 \tag{41}$$

$$\Delta t \leqslant O(2.9/N^2) \tag{42}$$

$$\Delta t \leqslant O(\Delta x^2). \tag{43}$$

Numerical Implementation of the Akers-Milewski Equation.

Due to the presence of linear and nonlinear terms in the Akers-Milewski equation, there is a stiffness problem with the numerical implementation, as seen in the CFL condition above. Thus, integrating factors are incorporated to minimize the stiffness of the equation. The derivation of the integrating factors method follows. First, convert the equation into Fourier space, where $\hat{u}$ denotes the Fourier transform of u.

$$\widehat{u}_t - c\widehat{u}_x + \hat{\mathscr{H}}\hat{u} - \hat{\mathscr{H}}\widehat{u_{xx}} - 3/2\widehat{uu_x} = 0 \tag{44}$$

$$\widehat{u}_t - c(ik)\hat{u} - i\,\mathrm{sign}(k)\hat{u} - i\,\mathrm{sign}(k)k^2\hat{u} = 3/2\widehat{uu_x} \tag{45}$$

where k is the wave number. Note that $(0.5\,u^2)_x = uu_x$. Therefore, $\widehat{uu_x} = \widehat{(0.5\,u^2)_x} = (ik)\widehat{0.5\,u^2} = (ik)\mathscr{F}[\mathscr{F}^{-1}(0.5\,\hat{u})^2] = \mathscr{N}(\hat{u})$, where $\mathscr{F}$ is the Fourier transform, $\mathscr{F}^{-1}$ is the inverse Fourier transform, and $\mathscr{N}(\hat{u})$ denotes the nonlinear equation. Using this

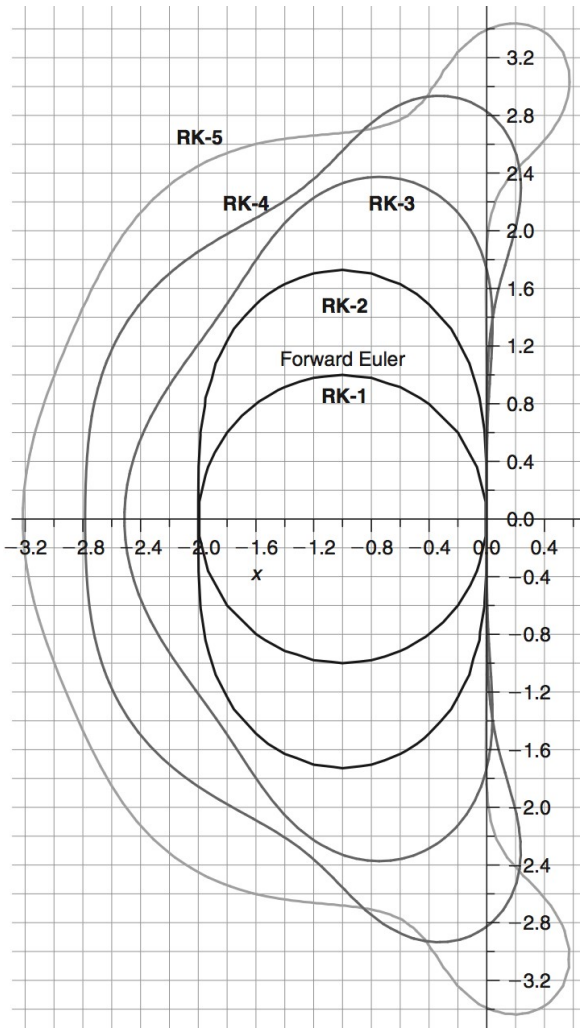

Figure 10. The plot shows the stability region for first-order through fifth-order Runga-Kutta methods [1]. The x-axis is Re($\lambda\Delta t$) and the y-axis is Im($\lambda\Delta t$).

in the equation yields

$$\widehat{u_t} - i[ck + \text{sign}(k)(1 + k^2)]\hat{u} = 3/2\mathscr{N}(\hat{u}). \tag{46}$$

Now multiplying both sides by $e^{\gamma t}$, where $\gamma \equiv -i[ck + \text{sign}(k)(1 + k^2)]$ yields

$$e^{\gamma t}\widehat{u_t} + e^{\gamma t}\gamma\hat{u} = 3/2\, e^{\gamma t}\mathscr{N}(\hat{u}). \tag{47}$$

Let $\mathscr{B} \equiv e^{\gamma t}\hat{u}$. Consequently, $\hat{u} = e^{-\gamma t}\mathscr{B}$. Also, note that $\frac{d}{dt}(\mathscr{B}) = \mathscr{B}_t = e^{\gamma t}\widehat{u_t} + e^{\gamma t}\gamma\hat{u}$, the left-hand side of Equation 47. Thus,

$$\mathscr{B}_t = 3/2\, e^{\gamma t}\mathscr{N}(e^{-\gamma t}\mathscr{B}) \tag{48}$$

a new PDE with only a nonlinear term. Thus, the linear stiffness might be removed, as is observed numerically.

The system of ODEs (Equation 46) and the version incorporating integrating factors (Equation 48) are implemented with a fourth order Runge-Kutta time-stepping algorithm. Note that the initial data being provided to the algorithm is generated from a Newton solver. Figure 11 shows the Cauchy error plots of the output. Since the data points run parallel to a line of slope four, this is an indication that the methods have been implemented correctly.

As mentioned, the integrating factors are incorporated in the equation to counter the effects of stiffness in the equation. Figure 12 shows a plot of N (the number of spacial points) vs Δt_{max}. Note that Δt_{max} is the maximum time step for which the system evolves stably. Larger time steps cause the evolution to become unstable. The plot of N vs Δt_{max} is done for both the original form of the equation and the version with integrating factors. The slope of the plot gives the CFL condition for the

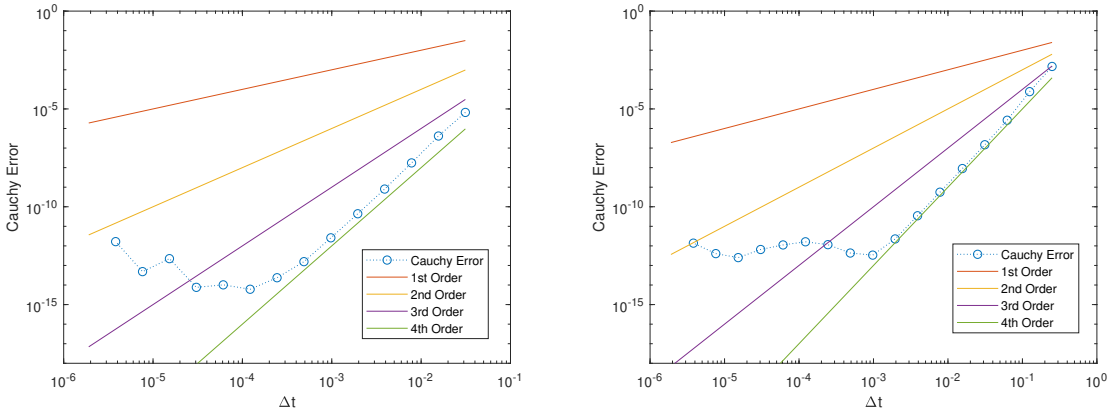

Figure 11. Cauchy Error of Akers-Milewski Equation using Fourth Order Runge-Kutta method. The figure on the left uses a direct implementation. The figure on the right uses integrating factors. The figures indicate that both sets of code have been implemented correctly

numerical method. The CFL conditions for the direct RK4 implementation and the RK4 with integrating factors are $\Delta t \leqslant O(\Delta x^{2.06})$ and $\Delta t \leqslant O(\Delta x^{1.25})$, respectively.

Spectral Stability Analysis of the Akers-Milewski Equation.

A derivation of the SSA method is first presented, followed by experiments and numerical results. Starting with the Akers-Milewski equation in a traveling frame of reference,

$$u_t - cu_x + \mathscr{H}u - \mathscr{H}u_{xx} - 3/2uu_x = 0. \tag{49}$$

First, consider the steady solution, solving

$$\cancelto{0}{\tilde{u}_t} - c\tilde{u}_x + \mathscr{H}\tilde{u} - \mathscr{H}\tilde{u}_{xx} - 3/2\tilde{u}\tilde{u}_x = 0. \tag{50}$$

Now, consider a perturbation to the system, $u(x,0) = \tilde{u}(x) + \delta v(x)$, where $\tilde{u}(x)$ is a steady solution, δ is a small constant, and $v(x)$ is a perturbation across the system. Next, consider the perturbed system, evolved in time: $u(x,t) = \tilde{u}(x) + \delta v(x)e^{\lambda t}$. Let this system be applied to Equation 49. [Note: the dependence of u and v on x and t

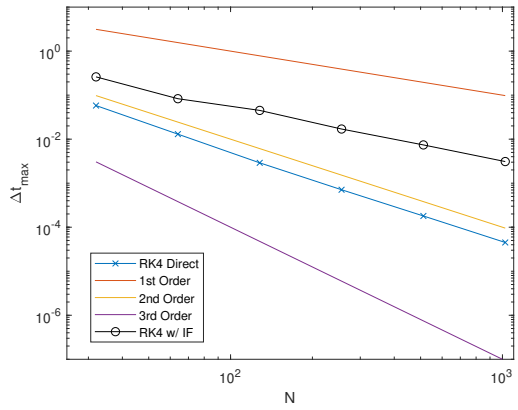

Figure 12. CFL Condition for Akers-Milewski Equation using Direct RK4 and RK4 with Integrating Factors. The RK4 Direct has a slope of 2.06, RK4 with Integrating Factors has a slope of 1.25.

will be dropped in the notation for brevity.]

$$\begin{aligned} 0 = \delta^0[&-c\tilde{u}_x + \mathscr{H}\tilde{u} - \mathscr{H}\tilde{u}_{xx} - 3/2\tilde{u}\tilde{u}_x] \\ &+ \delta^1[v\lambda e^{\lambda t} - cv_x e^{\lambda t} + \mathscr{H}ve^{\lambda t} - \mathscr{H}v_{xx}e^{\lambda t} - 3/2(\tilde{u}v_x e^{\lambda t} + \tilde{u}_x v e^{\lambda t})] \\ &+ \delta^2[-3/2vv_x e^{2\lambda t}]. \end{aligned} \tag{51}$$

Note that the δ^0 terms equal Equation 50, which equals zero. If the δ^2 term is ignored, then the system reduces to the following,

$$\lambda v = cv_x - \mathscr{H}v + \mathscr{H}v_{xx} + 3/2(\tilde{u}v_x + \tilde{u}_x v) \tag{52}$$

$$\lambda v = \left[c\frac{\partial}{\partial x} - \mathscr{H} + \mathscr{H}\frac{\partial^2}{\partial x^2} + 3/2\left(\tilde{u}\frac{\partial}{\partial x} + \tilde{u}_x\right)\right]v. \tag{53}$$

Now, consider all of the terms preceding v on the right side of the equation as an operator acting on v. Thus,

$$\lambda v = Av \tag{54}$$

where A is a linear operator as described. Equation 54 is a general spectral problem. Operator A is infinite dimensional. To approximate A, change both sides of the

equation into Fourier space.

$$\widehat{\lambda v} = \widehat{Av} \tag{55}$$

where $\widehat{Av}$ is truncated to a finite number of wave numbers. Now, consider F as a linear operator that transforms a vector in normal space into a vector in Fourier space. Applying F and an identity operator to the right side of the equation gives the following result,

$$\lambda \hat{v} = FAF^{-1}Fv. \tag{56}$$

Let FAF^{-1} be replaced by another linear operator, $\mathscr{A}$. Also, note that $Fv = \hat{v}$. Therefore,

$$\lambda \hat{v} = \mathscr{A}\hat{v}. \tag{57}$$

This equation is also in the form of a general spectral problem. Furthermore, operator A is similar to operator $\mathscr{A}$ (i.e., they have the same spectrum).

Although operator $\mathscr{A}$ is also unknown, there is a technique to determine its elements, column by column. First, note that $\widehat{Av} = \mathscr{A}\hat{v}$. Now, consider a perturbation vector, v_1, whose Fourier transform is $\hat{v}_1 = [1\ 0\ 0\ \cdots]^{\mathrm{T}} = e_1 =$ cannonical basis vector for the first coordinate. Therefore, $v_1 = \mathscr{F}^{-1}(\hat{v}_1)$. Now, plugging this vector into the right hand side of Equation 52 results in Av_1. Taking the Fourier transform of this result gives $\widehat{Av_1}$. Therefore,

$$\begin{aligned}\widehat{Av}_1 &= c(ik)\mathscr{F}[\mathscr{F}^{-1}(\hat{v}_1)] - (-i)\mathrm{sign}(k)\mathscr{F}[\mathscr{F}^{-1}(\hat{v}_1)] + (-i)\mathrm{sign}(k)(ik)^2\mathscr{F}[\mathscr{F}^{-1}(\hat{v}_1)] \\ &\quad + 3/2\tilde{u}(ik)\mathscr{F}[\mathscr{F}^{-1}(\hat{v}_1)] + 3/2(ik)\tilde{u}\mathscr{F}[\mathscr{F}^{-1}(\hat{v}_1)] \qquad (58) \\ &= c(ik)\hat{v}_1 + (i)\mathrm{sign}(k)(1+k^2)\hat{v}_1 + 3(ik)\tilde{u}\hat{v}_1. \qquad (59)\end{aligned}$$

Finally, note that $\mathscr{A}\hat{v}_1 = \mathscr{A}[1\ 0\ 0\ \cdots]^{\mathrm{T}} = \mathscr{A}_1$, the first column of $\mathscr{A}$. Therefore,

$$\mathscr{A}_1 = c(ik)\hat{v}_1 + (i)\mathrm{sign}(k)\hat{v}_1(1+k^2) + 3(ik)\tilde{u}\hat{v}_1. \tag{60}$$

Similarly,

$$\mathscr{A}_2 = c(ik)\hat{v}_2 + (i)\mathrm{sign}(k)\hat{v}_2(1+k^2) + 3(ik)\tilde{u}\hat{v}_2 \tag{61}$$

where $\hat{v}_2 = [0\ 1\ 0\ 0\ \cdots]^T$. This process is then repeated for each column of $\mathscr{A}$. This process is allowed because v_1 is a smooth function in real space. After $\mathscr{A}$ is fully determined, the eigenvalues are calculated via MATLAB's 'eig' function. Figure 13 shows a plot of the eigenvalues (real part vs. imaginary part).

Dynamic Stability Analysis of the Akers-Milewski Equation.

A derivation of the DSA method is first presented. Begin with the Akers-Milewski equation in a travelling frame of reference.

$$u_t - cu_x + \mathscr{H}u - \mathscr{H}u_{xx} - 3/2uu_x = 0 \tag{62}$$

Now consider a perturbation to the system, $u(x,0) = \tilde{u}(x) + \delta b(x)$, where $\tilde{u}(x)$ is a steady solution, δ is a small constant, and $b(x)$ is a perturbation across the system. Because $b(x)$ can take any form, a finite approximation is used. Consider,

$$b(x) = \sum_{j=1}^{N} \alpha_j v_j(x) \tag{63}$$

where α_j are constants, $v_j(x)$ are eigenfunctions, and N is the number of Fourier modes. This approximation of $b(x)$ presents an issue for estimating $Re(\lambda_{max})$. Since $b(x)$ is infinite dimensional, the N eigenfunctions are not a complete basis. Therefore, the actual $\mathbf{v}_{max}$ may not map onto the eigenspace. So, the largest eigenfunction, and

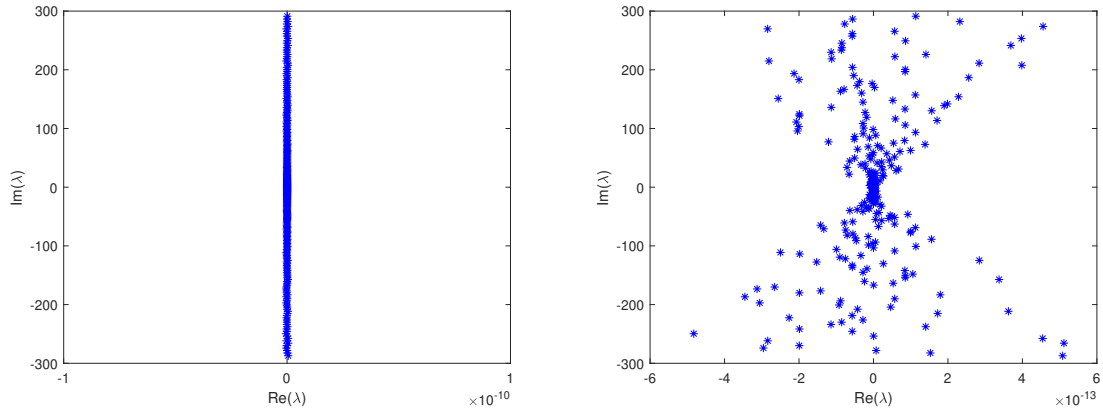

Figure 13. Steady Spectral Stability Analysis of the Akers-Milewski Equation: Eigenvalue Estimates. The figures on the left and right have different levels of zoom on the x-axis to show the relative size of the values.

associated eigenvalue, in the basis may not represent the actual maximum.

Returning to the derivation, plug the approximation of $b(x)$ into the perturbed system,

$$u(x,0) = \tilde{u}(x) + \delta \sum_{j=1}^{N} \alpha_j v_j(x) \tag{64}$$

The derivation from this point forward mimics that which was presented in the DSA section for the pendulum. The result is,

$$\log\|u(x,t) - \tilde{u}(x)\| \approx C + Re(\lambda_{max})t \tag{65}$$

where C is a constant and $Re(\lambda_{max})$ is the largest eigenvalue (real part) associated with an eigenfunction which is mapped to the eigenspace. Let $u(x,0) = \tilde{u}(x)(1+\delta)$. Therefore, the perturbation $\delta b(x) = \delta\tilde{u}(x)$. Using this initial condition and evolving the system with the numerical time stepper, the values of $\|u(x,t) - \tilde{u}(x)\|$ are collected as a function of time. When $Re(\lambda_{max}) \leqslant 0$, a plot of $\|u(x,t) - \tilde{u}(x)\|$ vs time should form a linear relationship due to an estimation error of the wave speed which is used to establish the frame of reference. Because of this estimation error, the value of $\|u(x,t) - \tilde{u}(x)\|$ will grow linearly with time. When $Re(\lambda_{max}) > 0$, a plot of

$\log \|u(x,t) - \tilde{u}(x)\|$ vs. time should form a linear relationship, whose slope is a lower bound for the value of $Re(\lambda_{max})$.

Figure 14 shows this type of plot for a depression wave (amplitude = -0.4). [Note that amplitude is defined as the distance from a flat wave to the largest peak/trough.] The plot on the left has linear axes, whereas the plot on the right has the y-axis in log scale. The plot on the left has an apparent linear relationship, whereas the plot on the right does not. Therefore, the data indicates that this depression wave is stable. However, the perturbation vector that was used, $\delta\tilde{u}(x)$, may or may not be in the same space as the eigenvector with the largest eigenvalue. Therefore, we cannot conclude that the wave solution is stable.

Figure 15 shows a similar set of plots for an elevation wave (amplitude = 0.4). The plot on the left does not show an apparent linear relationship, whereas the plot on the right does have a range in which there appears to be a linear relationship. It also shows periods of nonlinearity at the beginning and end of the plot. The nonlinearity at the beginning of the plot can be attributed to the non-maximum eigenvalues, whose effect is not yet diminished by the growth of time. The nonlinearity at the end of the plot can be attributed to the nonlinear terms $(o(\delta^2) + o(\delta^3) + \cdots)$, which were ignored in the derivation of this method.

As δ shrinks, the estimation of $Re(\lambda_{max})$ improves. Figure 16 shows the asymptotic estimation of $Re(\lambda_{max}) = 0.0963$. Since $Re(\lambda_{max}) > 0$, this elevation wave is unstable, as expected.

Comparison of Spectral Stability Analysis and Dynamic Stability Analysis.

Figure 17 shows a plot of the estimated $Re(\lambda_{max})$ values for SSA and DSA using several different amplitudes of elevation waves.

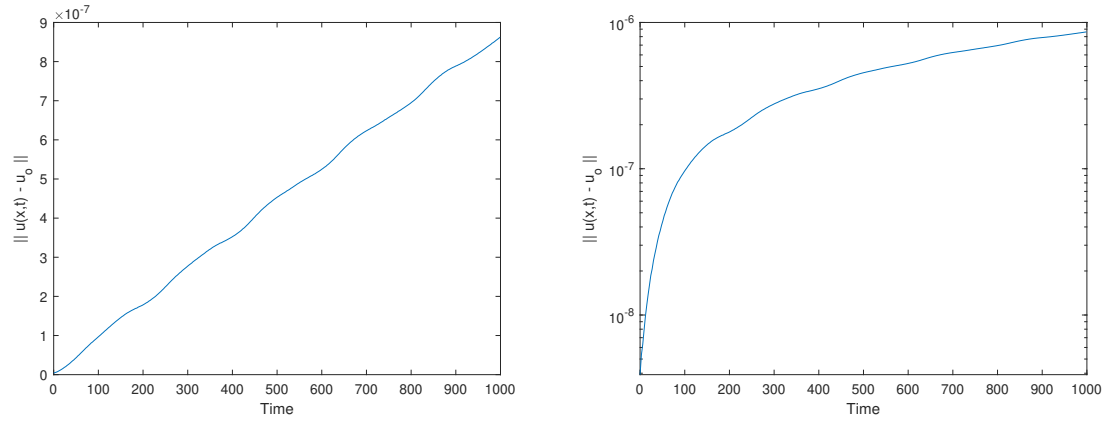

Figure 14. Dynamic Stability Analysis of a Depression Wave of the Akers-Milewski Equation. The figure on the left shows the linear plot of $\|u(x,t) - \tilde{u}(x)\|$ vs. time. The figure on the right shows the data with semi-log axes. The apparent linearity in the left figure indicates that the solution may be stable, though no conclusion can be made.

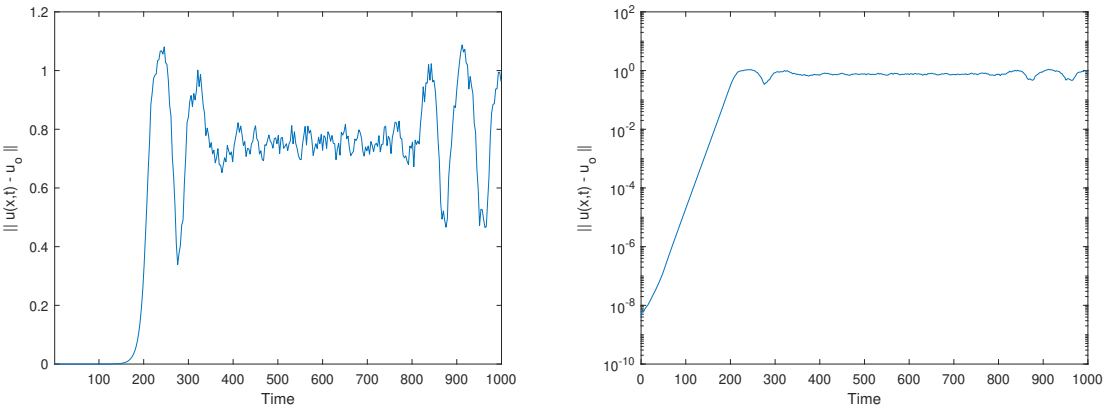

Figure 15. Dynamic Stability Analysis of an Elevation Wave of the Akers-Milewski Equation. The figure on the left shows the linear plot of $\|u(x,t) - \tilde{u}(x)\|$ vs. time. The figure on the right shows the data with semi-log axes. The apparent linearity in the right plot indicates that the solution is unstable. The slope of the linear portion provides a lower bound for $Re(\lambda_{max})$. For this plot, the slope of this linear portion is 0.0963.

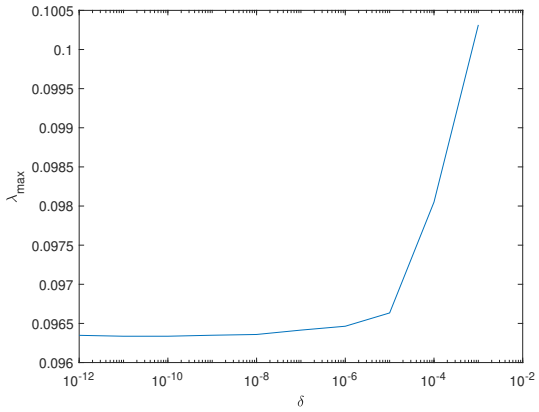

Figure 16. Dynamic Stability Analysis of an Elevation Wave of the Akers-Milewski Equation: Convergence of $Re(\lambda_{max})$. The accuracy of the estimation improves as δ gets smaller, converging to $Re(\lambda_{max}) = 0.0963$. This value is a lower bound for the true maximum eigenvalue.

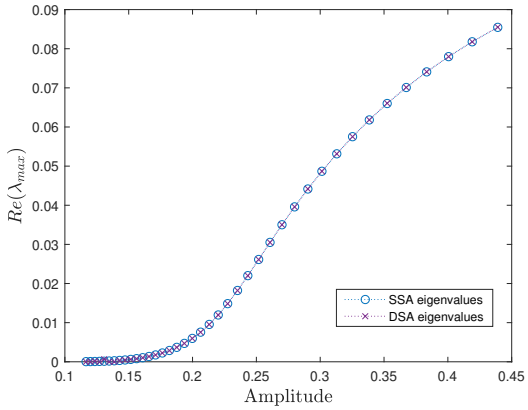

Figure 17. Spectral Stability Analysis vs. Dynamic Stability Analysis of Elevation Waves for Akers-Milewski Equation. The two methods show close agreement on eigenvalue estimation.

The SSA and DSA methods both have pros and cons. A clear advantage of the SSA is that it can reveal the full spectrum of a wave solution; giving both eigenvectors and eigenvalues. However, this comes at a computational cost. Calling the 'eig' function in MATLAB involves a QR factorization, which costs $O(N^3)$ flops.

One of the advantages of the DSA is the greater ease of implementing. As long as a time-stepping algorithm can be implemented for a traveling wave, the DSA can be used. Also, the computational cost is potentially less than that of the SSA. The CFL condition determines the computational cost of the time-stepper. For the Akers-Milewski equation, the CFL conditions were $\Delta t \leqslant O(\Delta x^{2.06})$ and $\Delta t \leqslant O(\Delta x^{1.25})$ for the direct RK4 and RK4 with integrating factors algorithms, respectively. Now, looking at this relationship in terms of time steps: $O(1/\Delta t) \sim O(1/\Delta x^{2.06}) = O(N^{2.06})$ and $O(1/\Delta t) \sim O(1/\Delta x^{1.25}) = O(N^{1.25})$. Additionally, a fast Fourier transform, which costs O(N log N) flops, is performed at each iteration of the algorithm. Thus, the total cost for the DSA is $O(N^{2.06})O(N \log N) = O(N^{3.06} \log N)$ flops for the direct RK4 algorithm and $O(N^{1.25})O(N \log N) = O(N^{2.25} \log N)$ flops for the RK4 with integrating factors algorithm. This cost assessment highlights the importance of using integrating factors, or some other method, to reduce the stiffness of the system. Despite potential cost savings, the DSA provides less information in the stability analysis. It provides a lower bound for the eigenvalue with the largest real part. If the estimate that it provides is positive, then the wave can be identified as being unstable. However, an estimate that is less than or equal to zero does not lead to any conclusion. Finally, the DSA allows the dynamics of the wave to be analyzed as it evolves.

2.4 Korteweg-de Vries Equation

The experiments in this section are not associated with stability. Rather, they focus on various methods for mitigating the stiffness of the equation. The methods explored are: integrating factors, Ruth splitting, and IMEX. As mentioned in the previous section, the stiffness of the equation directly affects the CFL condition, which determines the computational cost of the DSA algorithm. The following sections detail these methods.

The Korteweg-de Vries (KdV) equation is a PDE of waves in shallow water. Its basic form is,

$$u_t = u_{xxx} + uu_x \tag{66}$$

where u represents the height of the wave. Note that u is a function of x and t (i.e., $u(x,t)$). A transformation to change the traveling wave into a stationary wave could be performed, similar to that which was done with the Akers-Milewski equation. However, the form of Equation 66 is used in the following experiments. Various wave profiles can be used as the initial data for the KdV equation. The experiments in this section will use $\alpha\cos(x)$ for the initial data, where α is the amplitude of the wave.

Integrating Factors Applied to Korteweg-de Vries Equation.

The KdV equation has a linear term and a nonlinear term: u_{xxx} and uu_x, respectively. From Equation 66, first convert into Fourier space,

$$\hat{u}_t = \hat{u}_{xxx} + \widehat{uu}_x \tag{67}$$

$$= (ik)^3\hat{u} + (\widehat{u^2/2})_x \tag{68}$$

where k is the wave number. Note that $(0.5\,u^2)_x = uu_x$. Therefore, $\widehat{uu_x} = (\widehat{0.5\,u^2})_x = (ik)\widehat{0.5\,u^2} = (ik)\mathscr{F}[\mathscr{F}^{-1}(0.5\,\hat{u})^2] = \mathscr{N}(\hat{u})$, where $\mathscr{F}$ and $\mathscr{F}^{-1}$ are the Fourier trans-

form and inverse Fourier transform, respectively. Using this in the equation,

$$\hat{u}_t - (ik)^3\hat{u} = \mathscr{N}(\hat{u}) \tag{69}$$

Next, multiply both sides by $e^{\gamma t}$, where $\gamma = -(ik)^3$

$$e^{\gamma t}\hat{u}_t + e^{\gamma t}\gamma\hat{u} = e^{\gamma t}\mathscr{N}(\hat{u}) \tag{70}$$

Now, let $\mathscr{B} = e^{\gamma t}\hat{u}$. Consequently, $\hat{u} = e^{-\gamma t}\mathscr{B}$. Also, note that $\frac{\partial}{\partial t}(\mathscr{B}) = e^{\gamma t}\hat{u}_t + e^{\gamma t}\gamma\hat{u}$, the left hand side of Equation 70. Thus,

$$\mathscr{B}_t = e^{\gamma t}\mathscr{N}(e^{-\gamma t}\mathscr{B}) \tag{71}$$

the new PDE with only a nonlinear term. This PDE is implemented in MATLAB with a fourth order Runga-Kutta time-stepping algorithm. Figure 18 shows the Cauchy error of this implementation. The data matches up to a fourth order line, which indicates that the code has been implemented correctly. Also shown in Figure 18 is a CFL plot. The data shows the experimentally determined values of Δt_{max} for various space discretizations. A least squares fit of the data gives a CFL condition of: $\Delta t \leqslant O(N^{0.90})$. This is a remarkable improvement over the CFL condition for a direct RK4 implementation, which is $\Delta t \leqslant O(\Delta x^3)$. More plots were made for waves of varying amplitude with similar results.

Ruth Splitting Applied to the Korteweg-de Vries Equation.

The procedure presented by Forest and Ruth [30] is an example of a split-step method. Following their procedure, let $\alpha = 1-2^{1/3}$, $A = \frac{1}{2(1+\alpha)}$, $B = \frac{1}{1+\alpha}$, $C = \frac{\alpha}{2(1+\alpha)}$,

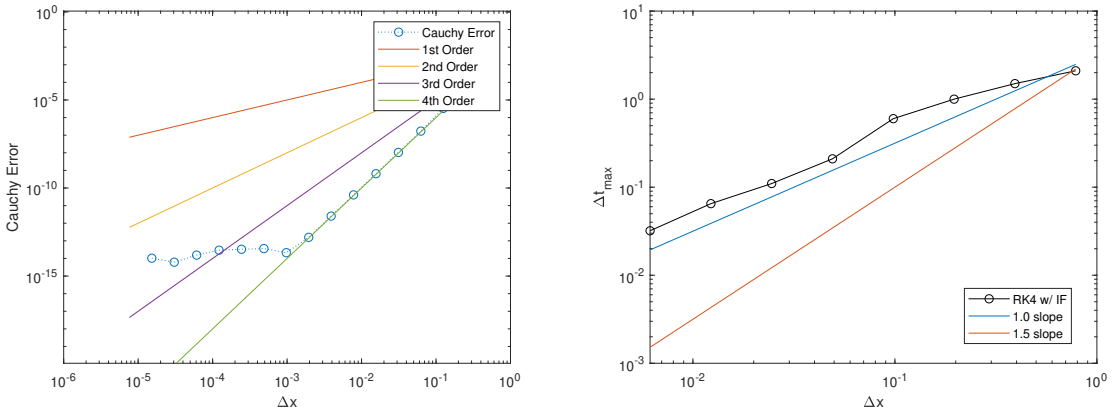

Figure 18. Cauchy Error and CFL Condition of the Korteweg-de Vries Equation with Integrating Factors. The initial condition is $u_o(x) = 0.1\cos(x)$. The figure on the left shows that the Cauchy data is fourth order, as expected for RK4. The figure on the right shows the CFL condition. Lines with slopes of 1.0 and 1.5 are given for reference. The data has a least squares fit of 0.90.

and $D = \frac{(\alpha-1)}{(\alpha+1)}$. Then,

$$u(t+\Delta t) = S_1(A\,\Delta t)S_2(B\,\Delta t)S_1(C\,\Delta t)S_2(D\,\Delta t)S_1(C\,\Delta t)S_2(B\,\Delta t)S_1(A\,\Delta t)u(t) \tag{72}$$

where S_1 is the nonlinear term of the KdV equation (i.e., $\hat{u}_t = (ik)\,\mathscr{F}[\mathscr{F}^{-1}(0.5\hat{u})^2]$) and S_2 is the linear term (i.e., $\hat{u}_t = (ik)^3\hat{u}$). Note that both terms are solved in Fourier space. S_1 is solved with a fourth order Runga-Kutta time-stepping algorithm. S_2 is solved directly. Figure 19 shows the Cauchy error and CFL plots for the KdV equation with Ruth splitting. The Cauchy error tracks closely to the fourth order line, indicating that the code is implemented correctly. A least squares fit of the data in the CFL plot gives a CFL condition of $\Delta t \leqslant O(\Delta x^{0.84})$.

Implicit-Explicit Methods Applied to Korteweg-de Vries Equation.

Ascher, Ruuth, and Wetton present equations for solving PDEs which include linear and nonlinear terms. These schemes are called Implicit-Explicit (IMEX) methods [9]. They present first-order through fourth-order schemes. The first-order and

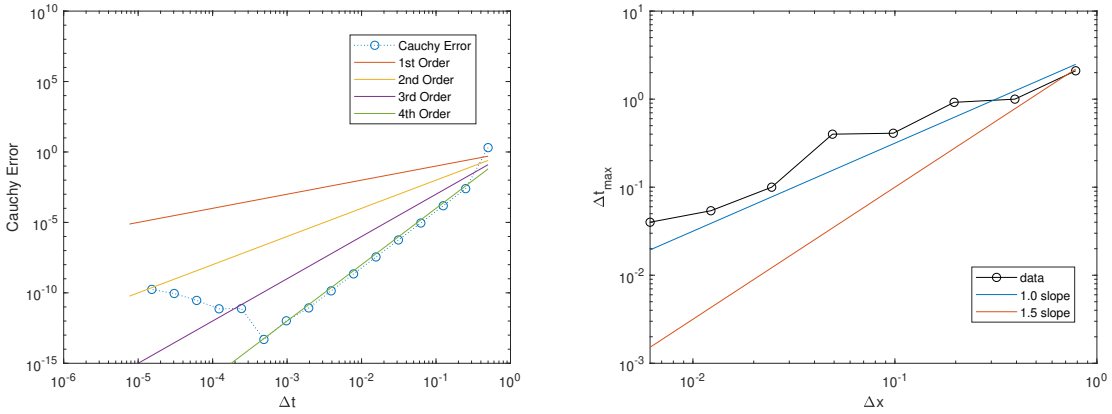

Figure 19. Cauchy Error and CFL Condition of the Korteweg-de Vries Equation with Ruth Splitting. The initial condition is $u_o(x) = 0.1\cos(x)$. The figure on the left shows that the Cauchy data is fourth order. The figure on the right shows the CFL condition. Lines with slopes of 1.0 and 1.5 are given for reference. The data has a least squares fit of 0.84.

second-order schemes are listed below.

First-order:

$$\frac{u^{n+1} - u^n}{\Delta t} = f(u^n) + Z_1 g(u^n) \tag{73}$$

Second-order:

$$\frac{u^{n+1} - u^n}{\Delta t} = 3/2 f(u^n) - 1/2 f(u^{n-1}) + Z_1/2[g(u^{n+1}) + g(u^n)] \tag{74}$$

where f and g are the nonlinear and linear terms, respectively, and Z_1 is a non-negative parameter.

The schemes were coded in MATLAB. The first-order and second-order schemes both performed as expected. Figure 20 shows the Cauchy error plots. The third-order and fourth-order schemes were attempted, but both were unstable. Kassam and Trefethen also found intermittent stability for IMEX schemes [36].

IMEX schemes are stable for any size time step. This was verified by increasing the size of the time steps for the second order IMEX scheme. It remained stable up to $\Delta t = 1.0$. Larger time steps were not attempted.

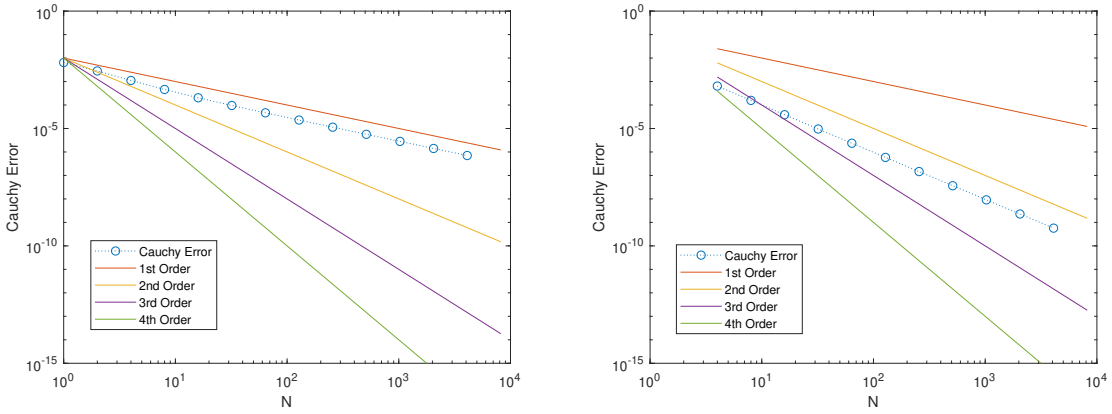

Figure 20. Cauchy Error for Korteweg-de Vries Equation with First-order and Second-order IMEX schemes. The figure on the left is the first-order IMEX scheme. The figure on the right is the second-order IMEX scheme

2.5 Vortex Sheet Equations

This section describes the vortex sheet problem and the associated equations of motion. This subject is treated in greater detail in [17][33][34]. Portions are repeated below for greater context.

Let there be two inviscid, incompressible, and irrotational fluids separated by an interface, Γ, as in Figure 21 [34]. The parameterized interface, Γ, is defined by $\mathbf{X}(\alpha, t) = (x(\alpha, t), y(\alpha, t))$, while $\mathbf{n}$ is the unit normal vector, $\mathbf{s}$ is the unit tangent vector, and α is the parameterization variable. The velocity, $\mathbf{u}$, on both sides of the interface are described by the Euler equations, as follows,

$$\mathbf{u}_{jt} + (\mathbf{u}_j \cdot \nabla)\mathbf{u}_j = -\frac{1}{\rho_j}\nabla(p_j + \rho_j g y) \tag{75}$$

$$\nabla \cdot \mathbf{u}_j = 0 \tag{76}$$

where the subscript j denotes fluid 1 or fluid 2, ρ is the fluid density, p is the fluid pressure, and g is the gravitational constant. The system is also governed by the

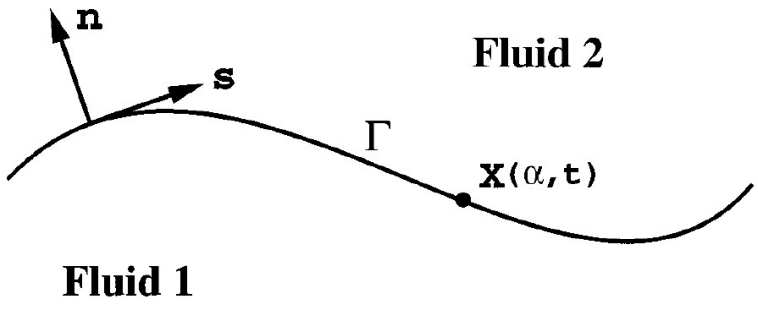

Figure 21. Diagram of a Fluid Interface for the Vortex Sheet Problem [33].

following boundary conditions,

$$[\mathbf{u}]_\Gamma \cdot \mathbf{n} = 0, \text{ the kinematic boundary condition} \tag{77}$$

$$[p]_\Gamma = \tau\kappa, \text{ the Laplace-Young boundary condition} \tag{78}$$

$$\mathbf{u}_j(x,y) \to (\pm V_\infty, 0) \text{ as } y \to \pm\infty, \text{ the far-field boundary condition} \tag{79}$$

where $[\cdot]_\Gamma$ denotes a jump from above to below Γ, τ is the surface tension, and *kappa* is the local curvature. V_∞ satisfies the equality $-\bar{\gamma}/2 = V_\infty$, where γ is the vortex sheet strength and $\bar{\gamma}$ is the average of γ in a period of the vortex sheet. While the normal component of fluid velocity, $U(\alpha)$, is continuous across Γ, the tangential velocity of the fluid, $V^F(\alpha)$, is typically discontinuous. The tangential velocity of the interface, V, is made up of the tangential fluid velocity, V^F and an arbitrary velocity value, V^A, by the relationship $V = V^F + V^A$. The selection of V^A establishes the parameterization. This type of interface is called a vortex sheet. The fluid velocity is defined by

$$U = \mathbf{W} \cdot \mathbf{n} \tag{80}$$

$$V^F = \mathbf{W} \cdot \mathbf{s} \tag{81}$$

where $\mathbf{W}$, the Birkhoff-Rott integral, is defined as

$$\mathbf{W} = \frac{1}{4i\pi}\text{P.V.}\int_0^{2\pi} \gamma(\alpha')\cot\frac{1}{2}(z(\alpha) - z(\alpha'))d\alpha' \tag{82}$$

where P.V. denotes the Cauchy principal value integral and $z(\alpha) = x(\alpha) + iy(\alpha)$ is the complexification of the interface position. The curve evolves according to the normal and tangential velocities by the following equation.

$$\mathbf{X}_t = U\mathbf{n} + V\mathbf{s}. \tag{83}$$

Now consider the interface curve described by the geometric variables θ and s_α rather than x and y, where θ is the tangent angle from the x-axis and s_α is the arclength metric. These variables are defined by the following relationships,

$$\theta = \tan^{-1}\left(\frac{y_\alpha}{x_\alpha}\right) \tag{84}$$

$$s_\alpha = \sqrt{x_\alpha^2 + y_\alpha^2}. \tag{85}$$

Consequently, given θ and s_α, $(x_\alpha, y_\alpha) = s_\alpha(cos(\theta), sin(\theta))$ from which (x, y) can be determined (up to a translation) by integration. The evolution of θ and s_α are described in the following equations,

$$\theta_t = \frac{U_\alpha + V\theta_\alpha}{s_\alpha} \tag{86}$$

$$(s_\alpha)_t = V_\alpha - \theta_\alpha U. \tag{87}$$

As mentioned previously, V^A is an arbitrary selection that determines the parameterization. For convenience, let V^A be chosen such that $V_\alpha = \theta_\alpha U$.

Next, let the length of the curve be defined by

$$L = 2\pi s_\alpha. \tag{88}$$

Then, the evolution of L is defined by

$$L_t = 2\pi(s_\alpha)_t \tag{89}$$

$$= 2\pi(V_\alpha - \theta_\alpha U). \tag{90}$$

By implementing the chosen definition of the tangential velocity, $V_\alpha = \theta_\alpha U$, the right hand side of Equation 90 falls out, except for the wavenumber $k = 0$. At this wavenumber, $V_\alpha = 0$ and $\theta_\alpha U$ equals its average value over the interval, i.e., $(\theta_\alpha U)_{k=0} = \frac{1}{2\pi}\int_0^{2\pi} \theta_\alpha U d\alpha$. Thus,

$$L_t = -\int_0^{2\pi} \theta_\alpha U d\alpha. \tag{91}$$

Finally, using this parameterization, the evolution of γ is

$$\begin{aligned}\gamma_t = &\frac{2\pi}{L}\theta_{\alpha\alpha} + \frac{2\pi}{L}\left((V - \mathbf{W}\cdot\mathbf{s})\gamma\right)_\alpha \\ &- 2A\left[\frac{2\pi}{L}\mathbf{W}_t\cdot\mathbf{s} + \frac{\sigma L}{2\pi}\sin(\theta) + \frac{\pi^2}{L^2}\gamma\gamma_\alpha - (V - \mathbf{W}\cdot\mathbf{s})(\mathbf{W}_\alpha\cdot\mathbf{s})\right]\end{aligned} \tag{92}$$

where A is the Atwood number and σ is the Bond number, defined as

$$A = \frac{\Delta\rho}{2\bar{\rho}} \tag{93}$$

$$\sigma = \frac{g}{k^2\tau} \tag{94}$$

where g is the gravitational constant and k is the typical wavenumber.

Numerical Implementation of the Vortex Sheet Equations.

A concise summary of the previous section shows that the pertinent equations to evolve the vortex sheet are

$$L_t = -\int_0^{2\pi} \theta_\alpha U d\alpha \tag{95}$$

$$\theta_t = \frac{U_\alpha + V\theta_\alpha}{s_\alpha} \tag{96}$$

$$\begin{aligned}\gamma_t = \frac{2\pi}{L}\theta_{\alpha\alpha} + \frac{2\pi}{L}\left((V - \mathbf{W}\cdot\mathbf{s})\gamma\right)_\alpha \\ - 2A\left[\frac{2\pi}{L}\mathbf{W}_t\cdot\mathbf{s} + \frac{\sigma L}{2\pi}\sin(\theta) + \frac{\pi^2}{L^2}\gamma\gamma_\alpha - (V - \mathbf{W}\cdot\mathbf{s})(\mathbf{W}_\alpha\cdot\mathbf{s})\right]\end{aligned} \tag{97}$$

The vortex sheet equations were implemented with a fourth order Runga-Kutta method. However, the implementation never reached fourth order. In fact, the Cauchy error plots never improved past first order. The main reason for this is the presence of the 'W_t' term. The steps of the Runga-Kutta methods require reference to variable values at previous time steps and previous algorithm steps. The 'W_t' term itself required a time-differences method to estimate its value. This, in effect, created a hybrid Runga-Kutta method that never performed well. Additionally, the computational cost is $O(N^2)$ flops per iteration. If the CFL condition is taken as that of the RK4 method, then $\Delta t \leqslant O(\Delta x^{1.5})$. Therefore, the cost of the scheme is $O(N^{3.5})$, which is greater than that of SSA ($O(N^3)$). These two factors combined made the vortex sheet equations too computationally expensive. Overall, the numerical implementation never allowed the waves to evolve long enough to obtain eigenvalue estimates. Therefore, the conformally-mapped Euler Equations were used as another system of equations to analyze overturned traveling waves.

2.6 Conformally-Mapped Euler Equations

Milewski, Vanden-Broeck, and Wang developed model equations for a two-dimensional solitary wave traveling on a fluid of infinite depth with gravity and capillary forces. Their model reformulates the Euler equations using a conformal map. The conformally-mapped Euler (CME) Equations [42] are:

$$X_\xi = 1 - \mathscr{H}(Y_\xi), \tag{98}$$

$$\Psi_\xi = \mathscr{H}(\Phi_\xi), \tag{99}$$

$$Y_t = Y_\xi \mathscr{H}\left(\frac{\Psi_\xi}{J}\right) - X_\xi\left(\frac{\Psi_\xi}{J}\right), \tag{100}$$

$$\Phi_t = \frac{\Psi_\xi^2 - \Phi_\xi^2}{2J} - Y + \frac{X_\xi Y_{\xi\xi} - X_{\xi\xi} Y_\xi}{J^{3/2}} + \Phi_\xi \mathscr{H}\left(\frac{\Psi_\xi}{J}\right), \tag{101}$$

where ξ is the parameterization variable, X *and* Y are the positional coordinates, Φ *and* Ψ are the velocity potential and its harmonic conjugate, respectively, and $J = X_\xi^2 + Y_\xi^2$. The CME equations in a moving frame of reference, coinciding with the speed of the wave, c, are

$$Y_t = Y_\xi \mathscr{H}\left(\frac{\Psi_\xi - cY_\xi}{J}\right) - X_\xi\left(\frac{\Psi_\xi - cY_\xi}{J}\right), \tag{102}$$

$$\begin{aligned}\Phi_t = &-\frac{1}{2}\left(\frac{\Psi_\xi^2 + \Phi_\xi^2}{J}\right) - BY + \frac{X_\xi Y_{\xi\xi} - X_{\xi\xi} Y_\xi}{J^{3/2}} + \Phi_\xi \mathscr{H}\left(\frac{\Psi_\xi - cY_\xi}{J}\right) \\ &+ \Psi_\xi\left(\frac{\Psi_\xi - cY_\xi}{J}\right) + \frac{c(X_\xi \Phi_\xi + \Psi_\xi Y_\xi)}{J},\end{aligned} \tag{103}$$

while the closures for X_ξ *and* Ψ_ξ remain unchanged. Note that the first set of CME equations are written specifically for a surface water wave with Bond number, B, equal to one. The CME equations written in a moving frame incorporate B as a variable.

III. Numerical Results

The goal is to determine the stability of several branches of waves from the CME equations. First, the numerical methods to calculate the eigenvalues of these waves via SSA and DSA are developed. Numerical problems with each method are addressed along with techniques to ameliorate the issues. Verification and validation experiments are used to estimate accuracy limits and create confidence in the implementation of the methods. The overall results will be presented in the next chapter.

3.1 Spectral Stability Analysis of the Conformally-Mapped Euler Equations

A derivation of the SSA method applied to the CME equations is long and tedious. The reader is directed to Appendix A for the detailed presentation.

Computed Spectrum vs. Exact Spectrum.

One validation of the SSA method is to compare the output from the code to the known, exact solution for flat, linear waves. The flat wave is generated by the Newton solver with an amplitude of zero. The linear wave is derived as follows. First, the nonlinear portions of the CME equations must be removed. Start by identifying the linear terms of the equations using small amplitude analysis. Let,

$$Y(\xi) = \delta Y_1(\xi) + O(\delta^2) \tag{104}$$

$$X_\xi(\xi) = 1 - \delta \mathscr{H}(Y_{1\xi}(\xi)) + O(\delta^2) \tag{105}$$

$$\Phi(\xi) = \delta \Phi_1(\xi) + O(\delta^2) \tag{106}$$

$$\Psi_\xi(\xi) = \delta \mathscr{H}(\Phi_{1\xi}(\xi)) + O(\delta^2). \tag{107}$$

Now, apply these definitions to the CME equations and identify the $O(\delta)$ terms as follows,

$$Y_t = (\delta Y_1)\mathscr{H}\left(\frac{\delta\mathscr{H}(\Phi_{1\xi}) - c\delta Y_{1\xi}}{J}\right) - (1-\delta\mathscr{H}(Y_{1\xi}))\left(\frac{\delta\mathscr{H}(\Phi_{1\xi}) - c\delta Y_{1\xi}}{J}\right) \tag{108}$$

$$= -\left(\frac{\delta\mathscr{H}(\Phi_{1\xi}) - c\delta Y_{1\xi}}{(\delta X_\xi)^2 + (\delta Y_{1\xi})^2}\right) + O(\delta^2) \tag{109}$$

$$= -\left(\frac{\delta\mathscr{H}(\Phi_{1\xi}) - c\delta Y_{1\xi}}{(1-\delta\mathscr{H}(Y_{1\xi}))^2 + (\delta Y_{1\xi})^2}\right) \tag{110}$$

$$= -(\delta\mathscr{H}(\Phi_{1\xi}) - c\delta Y_{1\xi}) \cdot \left[\frac{1}{(1 - \left(2\delta\mathscr{H}(Y_{1\xi}) - \delta^2\mathscr{H}(Y_{1\xi})^2 - \delta^2 Y_{1\xi}^2\right)}\right]. \tag{111}$$

Note that the bracketed portion on the right can be estimated with a geometric series: $\frac{1}{1-x} = \sum_{n=0}^{\infty} x^n$. Thus,

$$Y_t = -(\delta\mathscr{H}(\Phi_{1\xi}) - c\delta Y_{1\xi}) \cdot (1 + 2\delta\mathscr{H}(Y_{1\xi}) + O(\delta^2)) \tag{112}$$

$$= -\delta\mathscr{H}(\Phi_{1\xi}) + c\delta Y_{1\xi} + O(\delta^2). \tag{113}$$

Additionally,

$$(Y_l)_t = -\mathscr{H}(\Phi_\xi) + cY_\xi. \tag{114}$$

Continuing with the next equation,

$$\begin{aligned}\Phi_t = &-1/2\left(\frac{(\delta\Phi_{1\xi})^2 + (\delta\mathscr{H}(\Phi_{1\xi}))^2}{J}\right) - B\delta Y_1 \\ &+ \frac{(1-\delta\mathscr{H}(Y_{1\xi}))\delta Y_{1\xi\xi} - (1-\delta\mathscr{H}(Y_{1\xi}))_\xi \delta Y_{1\xi}}{J^{3/2}} \\ &+ \delta\Phi_{1\xi}\mathscr{H}\left(\frac{\delta\mathscr{H}(\Phi_{1\xi}) - c\delta Y_{1\xi}}{J}\right) \\ &+ \delta\mathscr{H}(\Phi_{1\xi})\left(\frac{\delta\mathscr{H}(\Phi_{1\xi}) - c\delta Y_{1\xi}}{J}\right) \\ &+ c\frac{(1-\delta\mathscr{H}(Y_{1\xi}))\delta\Phi_{1\xi} + \delta\mathscr{H}(\Phi_{1\xi})\delta Y_{1\xi}}{J}.\end{aligned} \tag{115}$$

Note that the geometric series expansion in the previous equation resulted in the J terms being eliminated from the linear equation. Thus,

$$\Phi_t = -B\delta Y_1 + \delta Y_{1\xi\xi} + c\delta\Phi_{1\xi} + O(\delta^2). \tag{116}$$

Consequently,

$$(\Phi_l)_t = -BY + Y_{\xi\xi} + c\Phi_\xi. \tag{117}$$

Now, converting these linear equations into Fourier space yields

$$\hat{Y}_t = -i\text{sign}(k)\hat{\Phi}_\xi + c\hat{Y}_\xi \tag{118}$$

$$= -i\text{sign}(k)(ik)\hat{\Phi} + c(ik)\hat{Y} \tag{119}$$

$$= |k|\hat{\Phi} + ick\hat{Y}, \tag{120}$$

$$\hat{\Phi}_t = -B\hat{Y} + \hat{Y}_{\xi\xi} + c\hat{\Phi}_\xi \tag{121}$$

$$= -B\hat{Y} + (ik)^2\hat{Y} + c(ik)\hat{\Phi} \tag{122}$$

$$= -B\hat{Y} - k^2\hat{Y} + ick\hat{\Phi}. \tag{123}$$

Now, combining these linear equations in matrix form yields

$$\begin{bmatrix} \hat{Y} \\ \hat{\Phi} \end{bmatrix}_t = \begin{bmatrix} ick & |k| \\ -(B+k^2) & ick \end{bmatrix} \begin{bmatrix} \hat{Y} \\ \hat{\Phi} \end{bmatrix} \tag{124}$$

$$= \mathbf{A} \begin{bmatrix} \hat{Y} \\ \hat{\Phi} \end{bmatrix}. \tag{125}$$

The eigenvalues of matrix A are,

$$\lambda = ick \pm i\sqrt{|k|(B+k^2)}. \tag{126}$$

Figure 22 shows a plot of these two spectra for a Crapper wave (B=0). Their similarity is an indication that the SSA code has been implemented correctly.

Removing Artifactual Eigenvalues.

The SSA method relies on matrix A being similar to matrix $\mathscr{A}$. However, in the implementation, matrix $\mathscr{A}$ is necessarily finite dimensional, whereas matrix A is infinitely dimensional. Therefore, matrix $\mathscr{A}$ is a numerical approximation of an infinite dimensional matrix $\tilde{\mathscr{A}}$. The assumption is that the most unstable eigenvalues from $\tilde{\mathscr{A}}$ will be present in $\mathscr{A}$. As the size of the dimensions for $\mathscr{A}$ increases, the resolution of $\Lambda_{\mathscr{A}}$ should increase. However, there are numerical artifacts which create eigenvalues that are not part of $\Lambda_{\tilde{\mathscr{A}}}$. Figure 23 shows $\Lambda_{\mathscr{A}}$ for different dimensions. The eigenvalues are not converging. This is true across the branch of waves and becomes more pronounced as the amplitude increases.

It is possible to discern between valid eigenvalues and spurious ones (ones that are not yet fully resolved) by analyzing the eigenvectors associated with each eigenvalue. Valid eigenvalues should have a smooth eigenvector, evidenced by larger support in the smaller frequency wavenumbers and smaller support in the higher frequency wavenumbers, relative to the grid size defined by N. Figure 24 shows the plots of a spurious eigenvector and a valid one.

Some simple code comparing the support at each wavenumber allows each eigenvector to be assessed for relative smoothness. Creating a threshold of allowed smoothness is a subjective decision and one that can be the subject of experimentation to determine the effect on the overall outcome of SSA. I found success by eliminating eigenvectors that violated the following rule:

$$\max_{k>3N/4} |\hat{y}(k)| \leqslant 10^{-3} \times \max_{k<3N/4} |\hat{y}(k)| \tag{127}$$

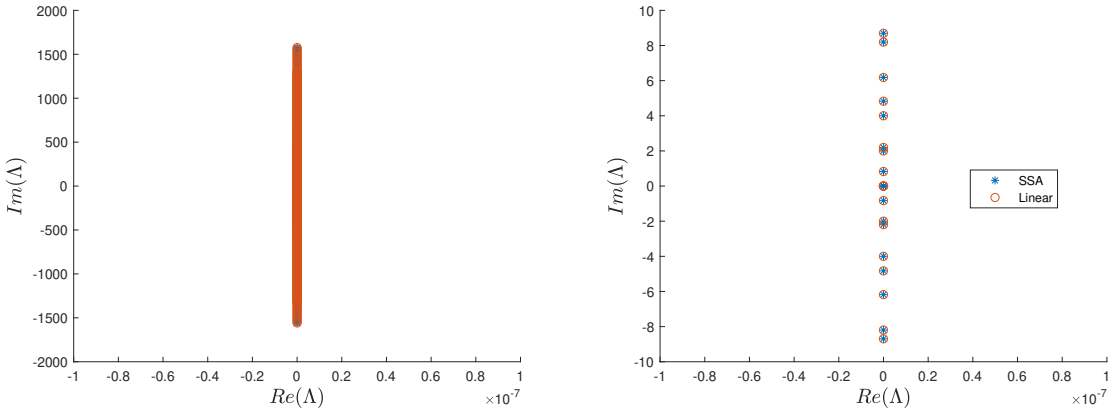

Figure 22. Computed Spectrum vs. Exact Spectrum of a Crapper Wave (B=0). The figure on the left shows the full spectrum. The figure on the right is zoomed in to show the overlay of individual spectra points.

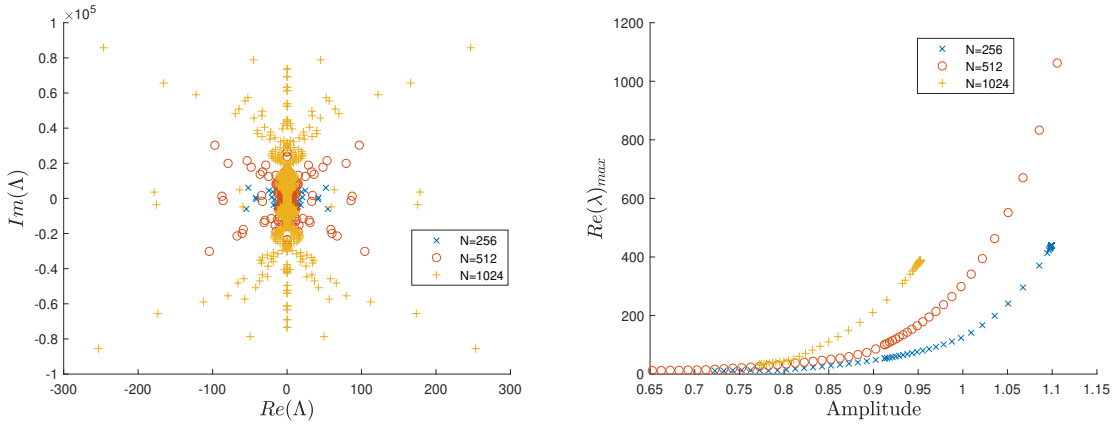

Figure 23. Computed Spectrum of Capillary Ripples via Spectral Stability Analysis with Numerical Artifacts. The figure on the left shows the spectrum for a solution to the CME equations (B=2, Amplitude=0.915) for multiple values of N. The figure on the right shows $Re(\lambda_{max})$ for a branch of MVW waves (B=2) at multiple values of N.

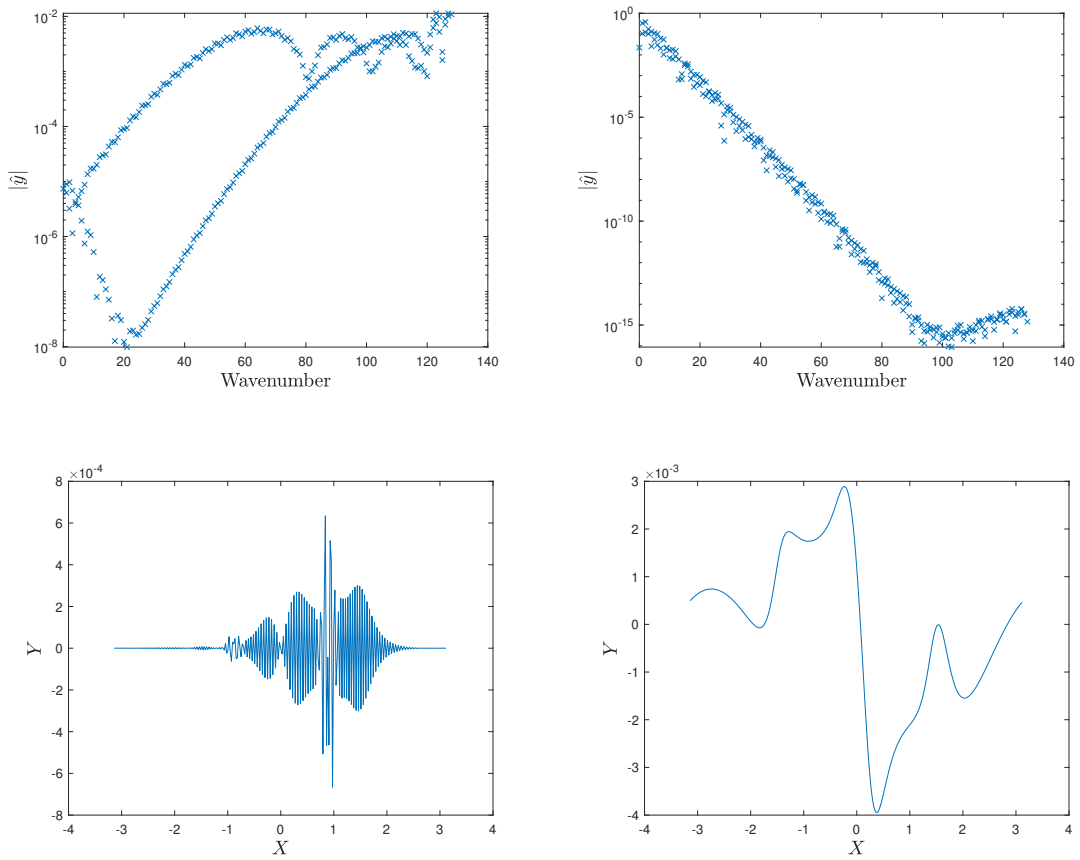

Figure 24. Spurious Eigenvector vs. Valid Eigenvector. The figure in the top left shows the support at each wavenumber of a spurious eigenvector. The figure in the top right shows the support at each wavenumber of a valid eigenvector. The figure in the bottom left shows a plot of the spurious eigenvector in real space. The figure in the bottom right shows a plot of the valid eigenvector in real space.

In other words, divide the wavenumbers into two groups. Group one consists of the 25% that have the highest frequency. Group two are all others. If the support at any of the wavenumbers in group one is more than 0.1% of the wavenumber with the largest support in group two, than the eigenvector and its associated eigenvalue are eliminated. Figure 25 shows the same spectrum as above but with the numerical artifacts removed. The plots show good convergence for multiple values of N, which provides additional verification for the SSA implementation.

SSA of Crapper Waves.

The Crapper wave is known to be stable to super-harmonic perturbations along its entire branch of waves[47]. Consequently, there should be no eigenvalues with positive real parts. Therefore, another validation method is to compare the SSA results for Crapper waves to this known maximum. Figure 26 shows the eigenvalues with maximum real part from SSA for a branch of Crapper waves. When the y-axis is in linear scale, the results appear to conform to the predicted stability. When the y-axis is in logarithmic scale, the eigenvalues have positive real parts that are less than 10^{-4}. This is used as a baseline for the accuracy threshold for SSA.

3.2 Dynamic Stability Analysis for Conformally-Mapped Euler Equations

The fourth order Runge-Kutta method is used as the numerical time stepper for the CME equations. For the experiments in this dissertation, a direct implementation of the CME equations is used. The complexity of the equations prevented the use of an integrating factors method or other methods to improve the stiffness of the equations to a stable, verified state. These methods can be the subject of future research efforts. The initial data for the time stepper comes from a Newton solver. Figure 27 shows the initial wave profile and the evolution of an overturned Crapper

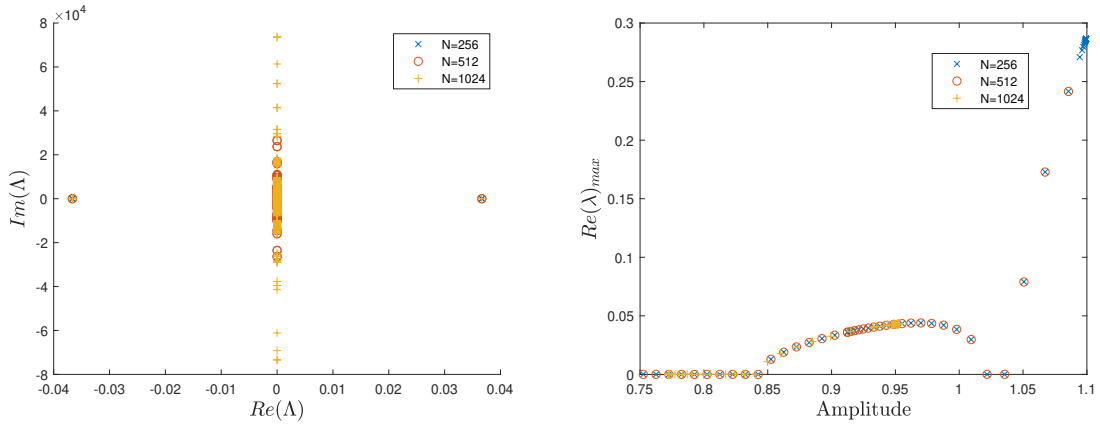

Figure 25. Computed Spectrum of Capillary Ripples via Spectral Stability Analysis with Numerical Artifacts Removed. The figure on the left shows the spectrum for a solution to the CME equations (B=2, Amplitude=0.915) for multiple values of N. The figure on the right shows $Re(\lambda_{max})$ for a branch of waves (B=2) at multiple values of N.

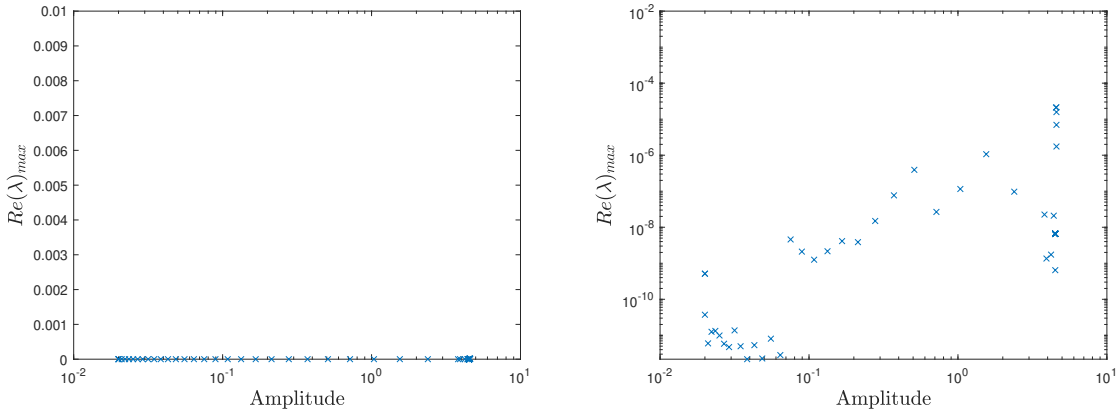

Figure 26. Computed $Re(\lambda_{max})$ for a Branch of Crapper Waves (B=0, N=256) via Spectral Stability Analysis. The figure on the left has the y-axis in linear scale. The figure on the right has the y-axis in log scale.

wave.

Eigenvalue Estimation via Dynamic Stability Analysis for Conformally-Mapped Euler Equations.

Most of the theoretical groundwork for DSA as a method for estimating eigenvalues was detailed in the Background chapter and will not be repeated here. It will suffice to repeat the result with pertinent variables from the CME equations. Start with a slightly perturbed initial condition: $Y_o = \tilde{Y}(1+\delta)$, where $\tilde{Y}$ is a solution to the CME equations from the Newton solver. Using this initial condition, evolve the system with the RK4 time stepper. The values of $\|(X,Y)-(X_o,Y_o)\|_\infty$ are collected as a function of time. Then,

$$\log\|(X,Y)-(X_o,Y_o)\|_\infty \approx C + Re(\lambda_{max})t \tag{128}$$

where C is a constant. When $Re(\lambda_{max}) \leqslant 0$, a plot of $\|(X,Y)-(X_o,Y_o)\|_\infty$ vs time should form a linear relationship due to an estimation error of the wave speed which is used to establish the frame of reference. Because of this estimation error, the value of $\|(X,Y)-(X_o,Y_o)\|_\infty$ will grow linearly with time. When $Re(\lambda_{max}) > 0$, a plot of $\log\|(X,Y)-(X_o,Y_o)\|_\infty$ vs. time should form a linear relationship, whose slope is a lower bound to the value of $Re(\lambda_{max})$.

CFL Condition.

From the SSA section above, it was shown that

$$\lambda = ick \pm i\sqrt{|k|(B+k^2)} \tag{129}$$

$$= O(i|k|^{3/2}) \tag{130}$$

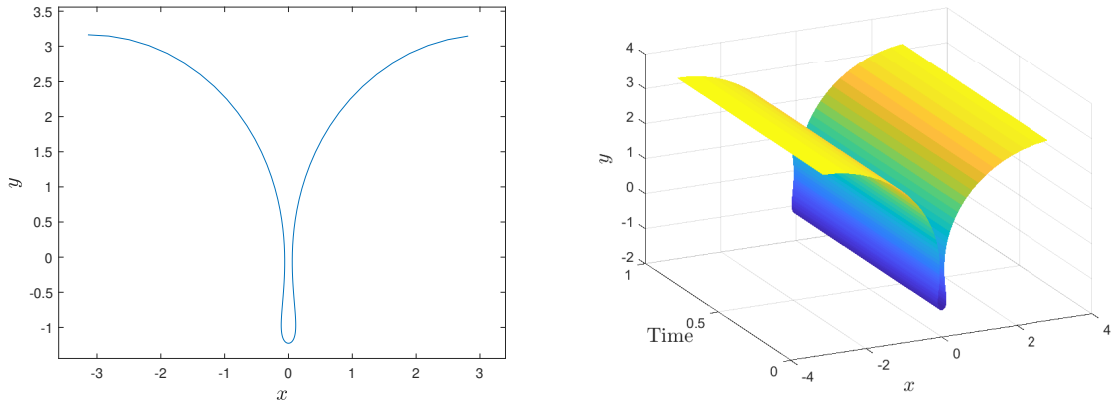

Figure 27. Crapper Wave Evolution. The figure on the left shows the intial wave profile from the Newton solver. The figure on the right shows the evolution using the RK4 time stepper. (N=128)

which are pure imaginary. Therefore, the fourth order Runge-Kutta method is stable for $-2.9 \leqslant \text{Imag}(\lambda)\Delta t \leqslant 2.9$. Therefore,

$$-2.9 \leqslant |k|^{3/2}\Delta t \leqslant 2.9. \tag{131}$$

Since $k \leqslant O(N)$,

$$-2.9 \leqslant O(N^{3/2})\Delta t \leqslant 2.9 \tag{132}$$

$$\Delta t \leqslant 2.9O(1/N^{3/2}) \tag{133}$$

$$\Delta t \leqslant O(\Delta\xi^{3/2}). \tag{134}$$

In order to confirm this result experimentally, Figure 28 shows a plot of the largest possible Δt values for different discretizations of two Crapper waves. The slope of the lines for the small amplitude wave and the large amplitude wave are 1.49 and 1.53, respectively. These results match closely with the predicted value of 1.5, which is one form of verification for the implementation of the time stepper.

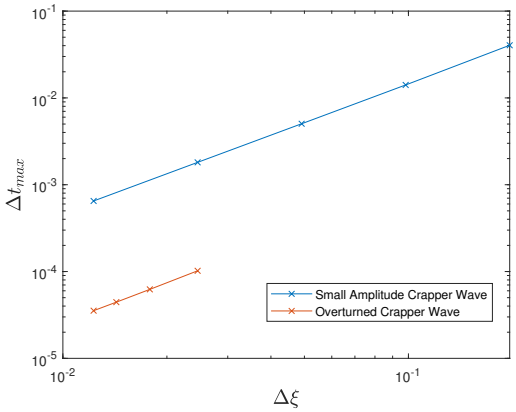

Figure 28. CFL Condition of Conformally-Mapped Euler Equations Using a Fourth Order Runga-Kutta Algorithm. The slope of the line determines the exponent of the CFL condition: $\Delta t \leqslant C(\Delta\xi)^{slope}$, where C is a constant. Two Crapper waves are plotted. The small amplitude wave (amp = 0.02) has a slope of 1.49. The large amplitude, overturned wave (amp = 4.58) has a slope of 1.53. Both values coincide closely with a theoretical value of 1.5.

Dealiasing.

The fourth order Runge-Kutta algorithm advances the wave in Fourier space. A finite number of Fourier modes are evolved. The modes are computed via a discrete Fourier transform. A consequence of this is that the higher frequency wave numbers (beyond the largest that is kept) are mapped to lower frequency wavenumbers. As the wave evolves in time, some of the higher frequency content becomes incorrectly inflated, leading to instability in the time-stepping algorithm. Figure 29 shows the growth in aliasing errors and the overall growth in error that results in the evolution of an overturned Crapper wave.

Various dealiasing methods are available. A pseudo-dealiasing method, and the one employed in my code, is simply setting the support for the highest frequency wavenumbers to zero. This is done at each time step. In doing this, care must be taken to ensure that the wavenumbers whose support are set to zero do not become necessary to characterize the profile of the wave as it evolves. Figure 30 shows the evolution of the same Crapper wave as above but with the 'dealiasing' code incorporated. As

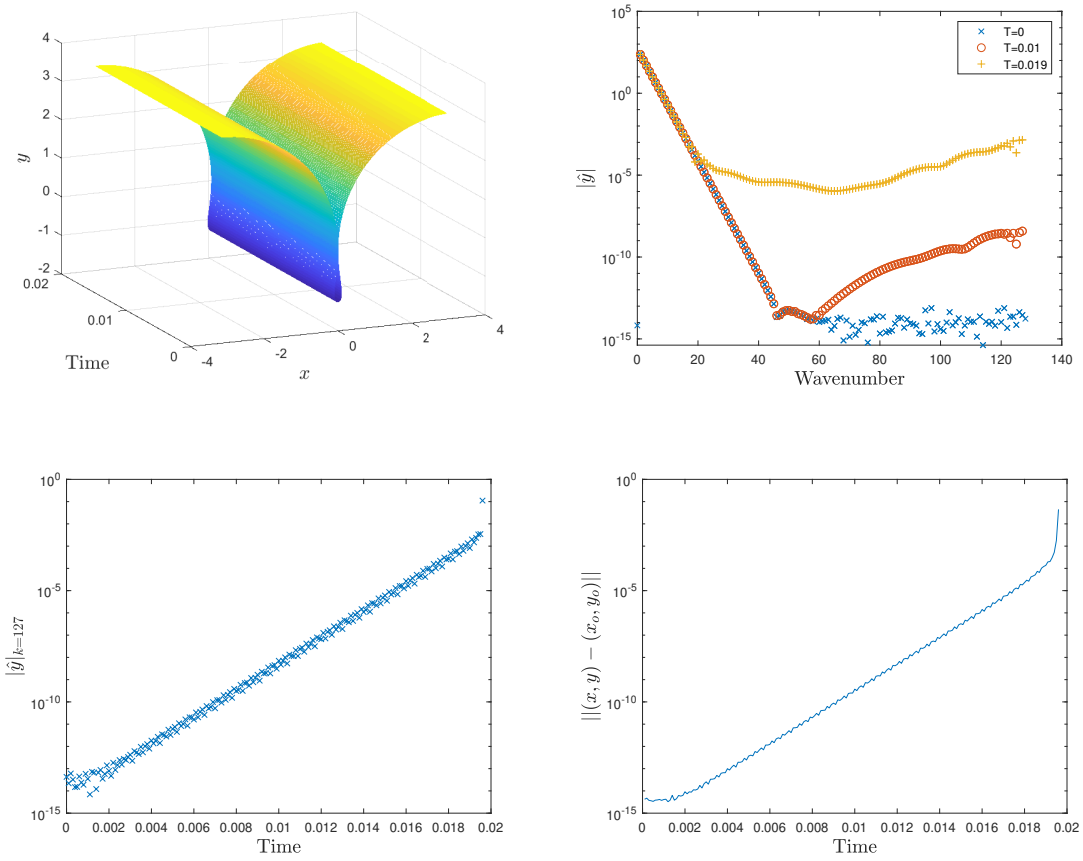

Figure 29. Aliasing Errors in the Time-Stepping Evolution of an Overturned Crapper Wave (N=256, amplitude=4.58). The figure in the top left shows the evolution of the overturned wave. The figure in the top right shows the support for each wavenumber at three time steps. The figure in the bottom left shows the support at the highest wavenumber as a function of time. The figure in the bottom right shows the overall growth in error.

can be seen in the figures, dealiasing effectively prevents errors from growing in the high-frequency range. This stabilizes the algorithm, allowing longer, more accurate simulations. Note that the evolution without dealiasing is unstable for a simulation time of less than 0.02 time units. Conversely, the evolution with dealiasing is stable after 1000 time units.

Dynamic Stability Analysis of Crapper Waves.

Figure 30 shows a long time evolution of a Crapper wave with nothing more than linear growth in the errors. Similar experiments were conducted for Crapper waves of other amplitudes with similar results. The linear growth in error can result from a combination of translation error from the wave speed and truncation error. Figure 31 shows the growth in error for the evolution of a Crapper wave with linear axes. It also includes a line with a slope of 10^{-14}. The tolerance for the Newton solver is 10^{-11}. Therefore, the growth in error is within the tolerance of the wave speed estimation.

DSA is not able to conclude that a wave is stable. It can only give a lower bound for $Re(\lambda_{max})$. However, the fact that the DSA code did not detect any instability in Crapper waves, which are known to be super-harmonically stable is an additional validation of the implementation of the method.

3.3 Spectral Stability Analysis vs Dynamic Stability Analysis for Wilton Ripples

SSA and DSA were run for various amplitudes of a Wilton ripple (solutions to the CME equations with B = 2.0). Figure 32 shows the profile and evolution of a Wilton ripple. Figure 33 shows the DSA error plot for a Wilton ripple lacking evidence of instability and one showing instability. Note that the instability does not present as a flat, linear line (in logarithmic scale). Rather it is an oscillating line with an

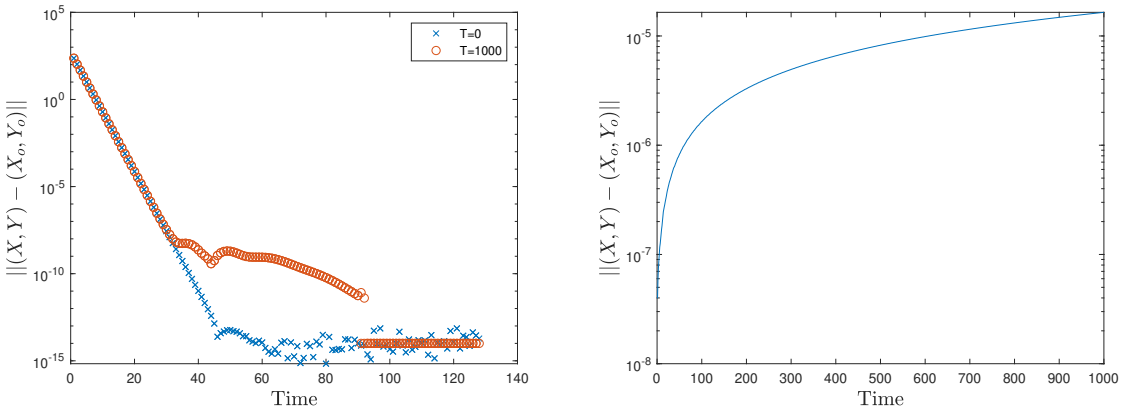

Figure 30. Evolution of a Crapper Wave with Dealiasing. The figure on the left shows the support at each wavenumber at the beginning and end of the simulation. The figure on the right shows the overall error.

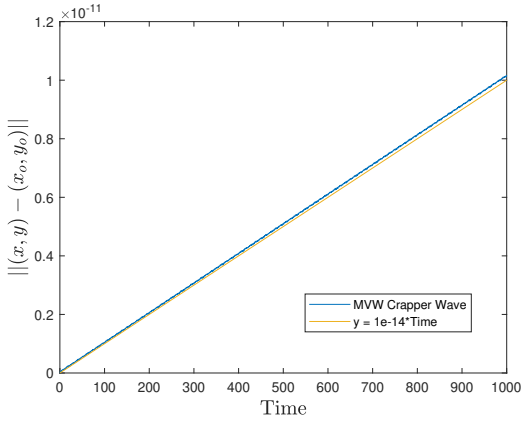

Figure 31. Linear Growth of Error for Dynamic Stability Analysis of Crapper Waves. The figure shows the error for the evolution of a Crapper Wave in linear scales. Also included is a linear plot of Time with a slope of 10^{-14}.

overall linear profile. Figure 34 shows the SSA and DSA estimations of $Re(\lambda_{max})$ for several amplitudes of Wilton ripples. The difference in their estimated values are within 10^{-3} of one another for all amplitudes. This is very good agreement and the final validation of the methods.

In conclusion, both DSA and SSA agreed in their predictions of stability/instability of various waves from the CME equations. They predicted the stability of Crapper waves to within 10^{-4} and agreed with one another within 10^{-3} on the eigenvalue estimates of Wilton ripples. The validation experiments were done for multiple waves of various amplitudes. The experiments establish high confidence in the methods within the stated accuracy ranges.

3.4 Instabilities of Gravity-Capillary Waves with B>0

The ultimate aim of this dissertation is to develop numerical methods and then determine the stability of overturned waves. Now that the methods are created, verified, and validated, the stability of these waves can be assessed. The DSA method takes significantly longer than SSA. A more thorough comparison of processing times is presented later. However, in order to maximize the number of waves being assessed, SSA was used for the majority of evaluations. DSA was used randomly to verify the SSA results.

In order to evaluate a large number of waves, a sequence of Bond numbers from zero to three was used. Initially, the Bond numbers included $B \in \{0,\ 0.1,\ 0.2, \cdots, 2.9\}$. A branch of waves for each Bond number was evaluated. While overturned waves are the area of focus, these branches naturally include many non-overturned waves as well. For regions with interesting results, additional branches of waves were evaluated in order to create greater fidelity. A 3-D plot of Bond number vs. Amplitude vs. $Re(\lambda_{max})$ create a smooth "surface of instability."

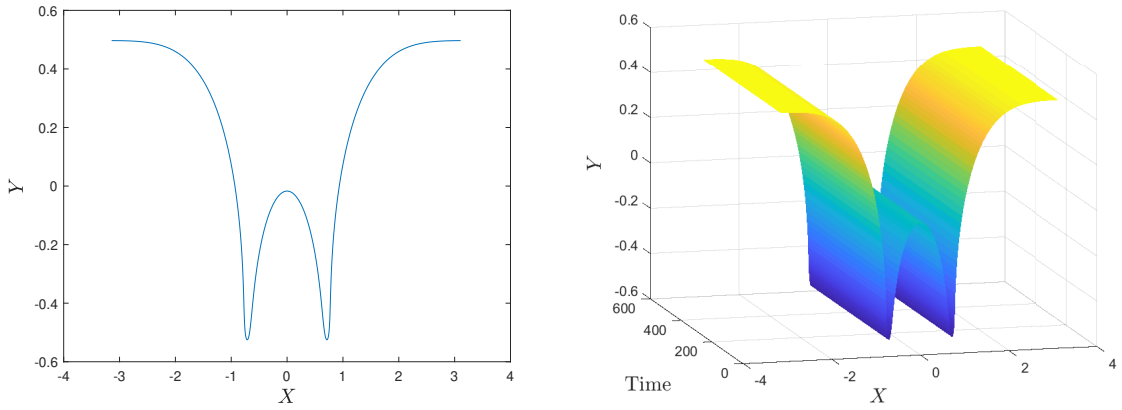

Figure 32. Wilton Ripple (B=2, N=256, Amplitude = 1.02). The figure on the left shows the initial wave profile. The figure on the right shows the time evolution of the wave.

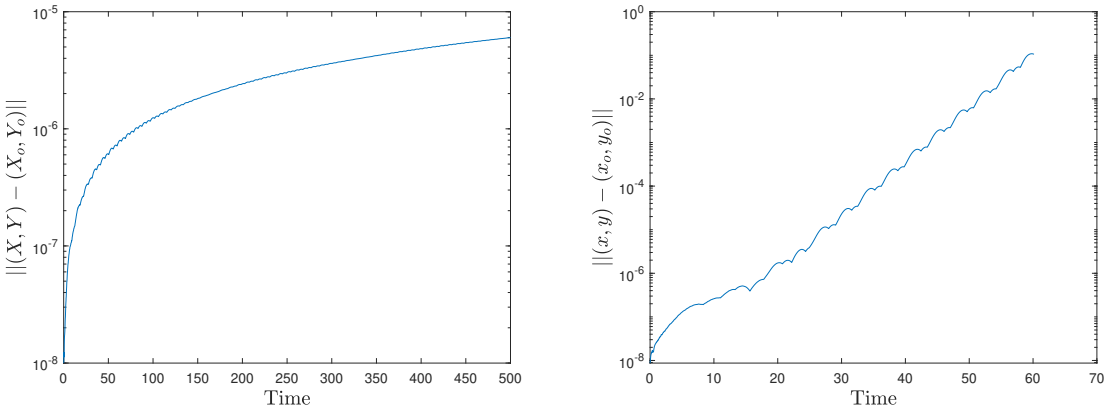

Figure 33. Dynamic Stability Analysis of Wilton Ripples (B=2, N=256). The figure on the left shows the DSA error plot of a Wilton ripple (amplitude=1.02) with linear, rather than exponential, growth in errors. The figure on the right shows the DSA error plot of a Wilton ripple (Amplitude=1.1) with evidence of instability.

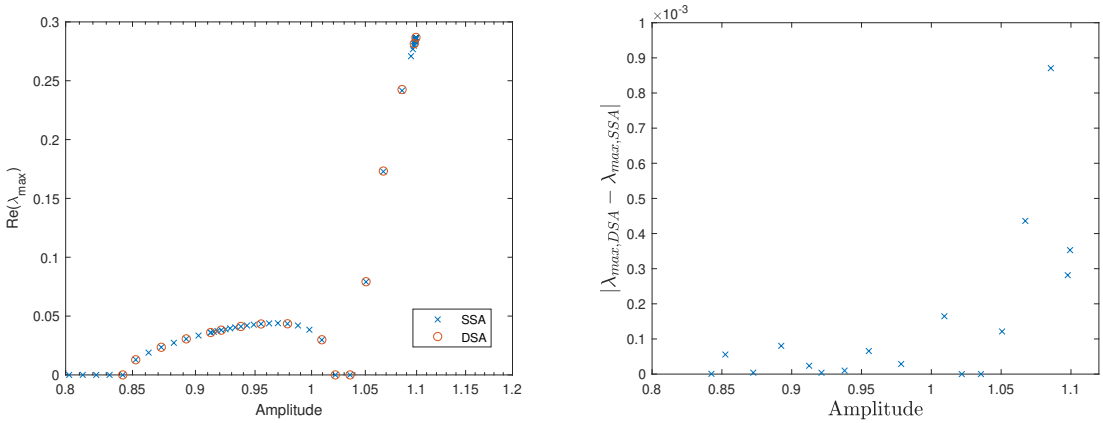

Figure 34. Spectral Stability Analysis vs. Dynamic Stability Analysis of Wilton Ripples (B=2, N=256). The figure on the left shows the SSA and DSA estimations of $Re(\lambda_{max})$ for several amplitude waves. The figure on the right shows the difference between the estimated values of SSA and DSA.

IV. Results

In this chapter, the stability analysis of gravity-capillary waves is presented. It is important to note that all experiments are performed with super-harmonic perturbations. Therefore, when results state that a given wave is stable, it is only referring to stability with respect to super-harmonic perturbations; not sub-harmonic perturbations. Stability with respect to sub-harmonic perturbations is addressed in the chapter for future research. Additionally, any stability conclusions are subject to the caveat that it is spectral stability. A comparison of SSA and DSA is also given.

4.1 Stability of Gravity-Capillary Waves

Initially, the Crapper waves (B=0) and Wilton ripples (B=2.0) were evaluated. These branches of waves were used for the verification and validation of SSA and DSA in the previous section. Crapper waves are already known to be stable. However, the stability of overturned Wilton ripples was unknown. Therefore, it is worthwhile to restate the results for the Wilton ripples. Figure 35 shows the areas of stability and instability for this branch of waves. It is interesting to observe that the Wilton ripples with smaller amplitudes are spectrally stable. As the amplitude increases beyond 0.85, they become unstable. However, there is a narrow range of waves with amplitudes between 1.02 and 1.03 which are stable. Beyond these amplitudes, the waves become increasingly unstable. The overturned Wilton ripples are in this region of unstable waves. Both SSA and DSA were in agreement for these results.

SSA was then run on branches of gravity-capillary waves with $B \in \{0,\ 0.1,\ 0.2, \cdots, 2.9\}$. Figure 36 shows the results of these experiments. The first, immediate observation is that all branches of waves with $B < 2.0$ are stable. Each of these branches includes overturned waves. Thus, in addition to the overturned Crapper wave, there

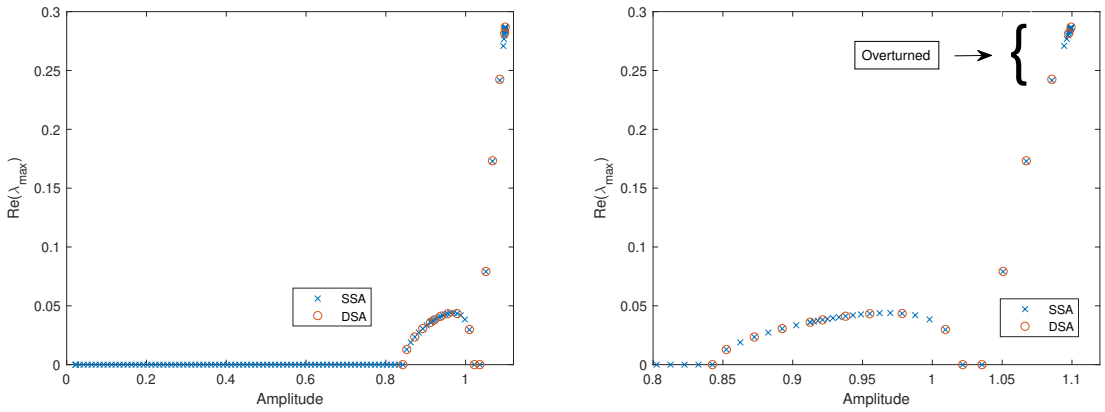

Figure 35. Spectral Stability Analysis vs. Dynamic Stability Analysis of Wilton Ripples (B=2, N=256). The figure on the left shows the SSA and DSA estimations of $Re(\lambda_{max})$ for the whole range of amplitudes. The figure on the right shows the results for those waves with larger amplitude. The overturned waves are identified in the right figure.

are several other overturned gravity-capillary waves that are stable to super-harmonic perturbations. Figure 37 shows the results of DSA applied to an overturned wave with $B = 1.9$. This experiment supports SSA's result of stability.

Another observation from Figure 36 is that there are "bubbles of instability" on the branches of waves approximately in the range of $2.0 \leqslant B \leqslant 2.5$. It is helpful to see the shape of these bubbles in greater detail. Therefore, branches of waves were investigated with Bond numbers between 2.0 and 2.99 with increments of 0.01. The resulting plot is shown in Figure 38. This plot overall depicts a "surface of instability." Within it, there are a few uniquely shaped "bubbles of instability." There is also a "wall of instability." All gravity-capillary waves (with $B \geqslant 2.0$) become unstable when their amplitudes reach this wall. The threshold of this wall changes for each branches of waves. The wall begins at an amplitude of about 1.04 for the branch of waves with $B = 2.0$. The threshold gradually changes to an amplitude of about 0.71 for the branch of waves with $B = 2.99$. This figure graphically represents my unique contribution to the mathematical community.

The branch of waves with $B = 1.99$ was also investigated to see if the "bubbles of

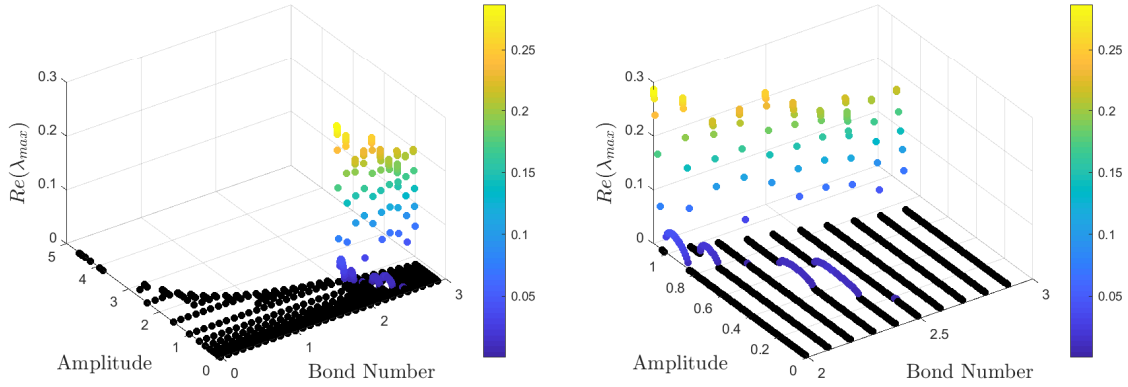

Figure 36. Stability of Gravity-Capillary Waves. The figure on the left shows the stability results for the branches of waves on the entire range of Bond numbers investigated ($0 \leqslant B \leqslant 2.9$). The figure on the right only shows the results for those branches of waves with larger Bond numbers ($2.0 \leqslant B \leqslant 2.9$). The waves that are stable are marked with a black dot. The waves with an instability are marked with a colored dot.

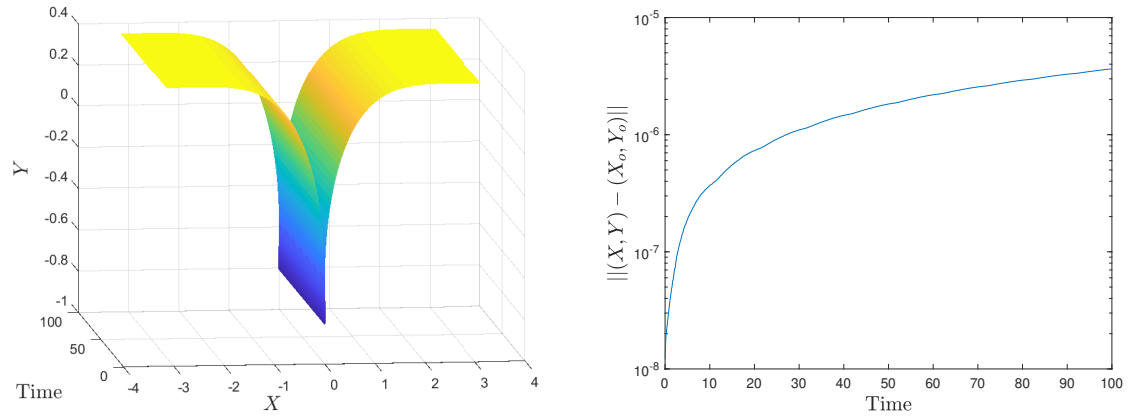

Figure 37. Dynamic Stability Analysis of an Overturned Gravity-Capillary Wave (B=1.9, N=256, Amplitude=1.16). The figure on the left shows the evolution of the wave. The figure on the right shows the error.

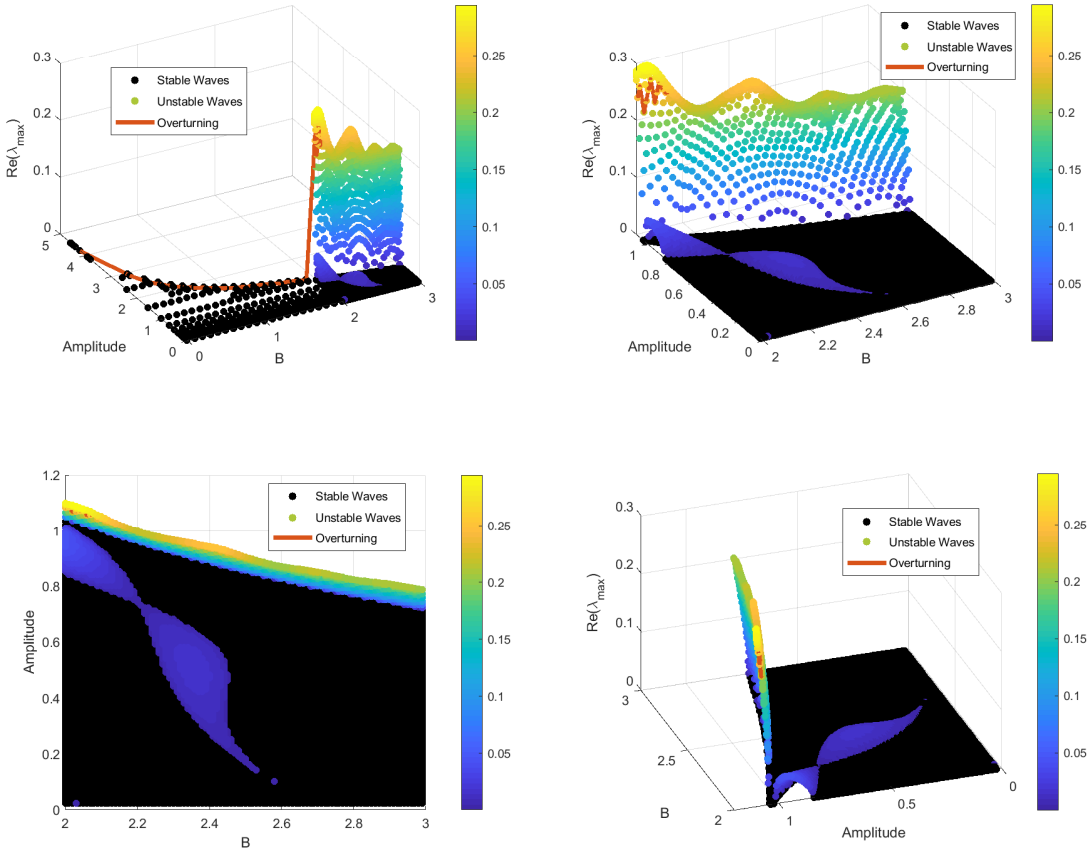

Figure 38. "Surface of Instability" for Gravity-Capillary Waves. The figure in the top right shows the Surface of Instability for the entire region of waves investigated. The other three figures show different views of the Surface of Instability for those waves with $2.0 \leqslant B \leqslant 2.99$. The red line shows where the waves begin to overturn on the branches.

instability" extend into the region of $B < 2.0$. This entire branch is also stable. Thus, all branches of gravity-capillary waves with $B \geqslant 2$ have waves that are unstable. All overturned waves in this region are unstable. All branches of waves with $B < 2$ are stable on the entire branch.

4.2 Spectral Stability Analysis vs Dynamic Stability Analysis

SSA and DSA (as they are coded for this dissertation) were both developed as a means to determine the instability of gravity-capillary waves. This section compares the two methods. First, the computation time is compared, followed by some general pros and cons of each method.

Computation Time.

For SSA, the computational demand is dominated by the call to MATLAB's 'eig' function. This function involves a QR iteration, which uses $O(N^3)$ flops. Fortunately, this part of the code is only executed one time per wave. Thus, the overall computational demand is,

$$\text{Cost}_{SSA} = O(N^3) \text{ flops} \tag{135}$$

$$= C_1 N^3 \text{ flops} \tag{136}$$

where C_1 is a constant. Now, assume that the computational time is proportional to the number of flops. Therefore,

$$\text{Time}_{SSA} = \tilde{C}_1 N^3 \tag{137}$$

where $\tilde{C}_1$ is a constant.

The DSA code is computationally dominated by several calls to MATLAB's 'fft'

and 'ifft' functions, which use $O(N\ logN)$ flops per function call. This code is repeated for each time step. Thus,

$$\text{Cost}_{DSA} = O(N\ logN) \times M \text{ flops} \tag{138}$$

where M is the number of time steps. Now,

$$M = \frac{T}{\Delta t} \tag{139}$$

where T is the total time of the simulation and Δt is the size of each time step. Note that the CFL condition dictates that $\Delta t \leqslant O(1/N^{3/2})$. Therefore,

$$\text{Cost}_{DSA} = O(N\ logN) * O(TN^{3/2}) \text{ flops} \tag{140}$$

$$= O(TN^{2.5} logN) \text{ flops} \tag{141}$$

$$= C_2 TN^{2.5} logN \text{flops} \tag{142}$$

where C_2 is a constant. Converting this to computational time gives,

$$\text{Time}_{DSA} = \tilde{C}_2 TN^{2.5} logN \tag{143}$$

where $\tilde{C}_2$ is a constant. Using these definitions, it is possible to determine T as a function of N so that SSA and DSA are comparable computationally.

$$\text{Time}_{DSA} = \text{Time}_{SSA} \tag{144}$$

$$\tilde{C}_2 TN^{2.5} logN = \tilde{C}_1 N^3 \tag{145}$$

$$T(N) = \left(\frac{\tilde{C}_1}{\tilde{C}_2}\right)\left(\frac{\sqrt{N}}{logN}\right) \tag{146}$$

Assume that $\tilde{C}_1/\tilde{C}_2$ is $O(1)$. Therefore,

$$T(N) \approx \frac{\sqrt{N}}{logN} \tag{147}$$

The following table gives values of T for several values of N based on this analysis.

N	**T**
128	1.6
256	2.0
512	2.5
1024	3.2

Figure 39 shows a plot of N vs T. This figure includes the theoretical values derived above. It also includes the experimentally determined values for small amplitude Crapper waves and large amplitude Crapper waves. Experiments were run on the Wilton ripples with similar break-even times. These two experimentally determined lines give an upper and lower bound for the break-even times between SSA and DSA for gravity-capillary waves. The figure also includes the experimentally determined simulation time required to recover the eigenvalue for large-amplitude Wilton ripples. This gives a lower bound for the necessary time. By comparison, there are no instances (in the bounds used) in which DSA is computationally faster than SSA. If extrapolation of the plot proved to be valid, then DSA would become comparable to SSA when $N \approx 6000$.

As mentioned previously, DSA was implemented directly with the RK4 scheme, without any stiffness reducing methods. If the integrating factors method were used, the CFL condition would likely become $\Delta t \leqslant O(1/N)$, which would give DSA an overall computational time of,

$$\text{Time}_{DSA/IF} = O(TN^2 logN) \tag{148}$$

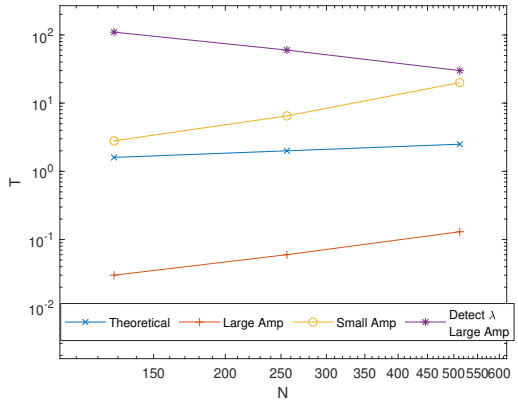

Figure 39. SSA vs DSA: Break-Even Analysis. The figure shows the time units (T) for DSA so that it has the same processing time as SSA, as determined experimentally. A line for small amplitude waves and large amplitude waves is given; providing bounds for the break-even simulation time, T. It also has the theoretical values for reference. Additionally, the simulation time required to recover the eigenvalues for large amplitude waves is given. Because these lines do not cross, DSA is never computationally faster than SSA within the values of N used.

and a theoretical break-even time of,

$$T(N) \approx \frac{N}{logN} \tag{149}$$

which would make DSA more computationally competitive.

Pros and Cons.

One of the advantages of SSA is that it gives the full spectrum (truncated to N and minus the spurious ones) of the eigenvalues, whereas DSA only gives a lower bound for the eigenvalue with the largest real part. Additionally, SSA gives the eigenvectors associated with each eigenvalue; DSA does not. The main advantage of DSA is that it presents the dynamics of the wave as it evolves. Should the wave change into a different, stable wave, DSA would show this evolution. Figure 40 shows the dynamics of an unstable Wilton ripple as the instability is manifested. This wave does not evolve into a different, stable wave.

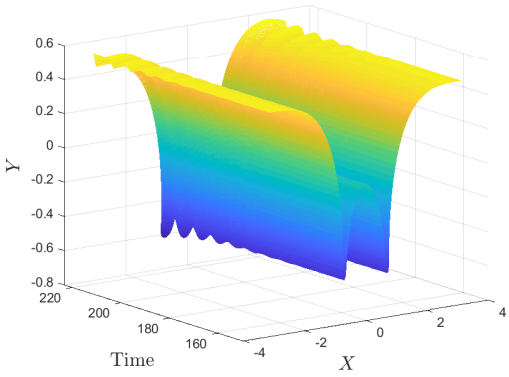

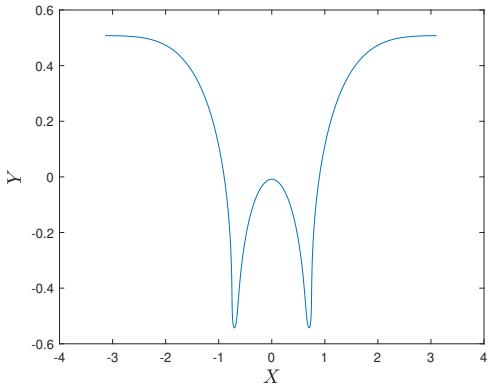

(a) T=0

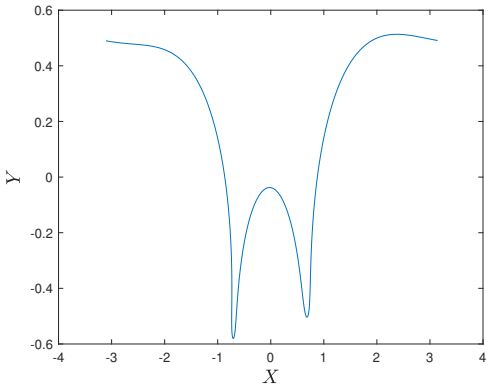

(b) T=215

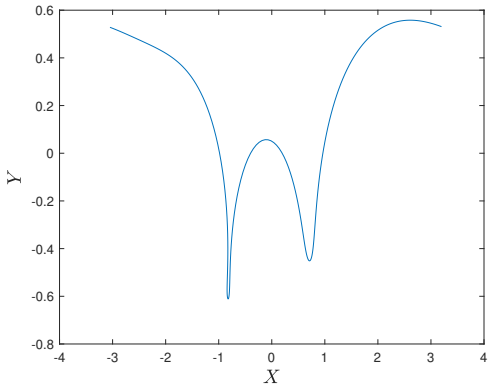

(c) T=223

Figure 40. Dynamics of an Unstable Wilton Ripple (B=2, N=256, Amp=1.05). The figure in the top left shows a mesh plot of the ripple as it evolves. The other three plots show the profile of the ripple at different times.

V. Future Research

The research in this dissertation naturally lends itself to future research avenues. An initial area would be analyzing the stability of gravity-capillary waves to sub-harmonic perturbations. The research in this dissertation exclusively used super-harmonic perturbations. Super-harmonic perturbations have a period equal to (or an integer multiple of) the wave being perturbed. Sub-harmonic perturbations have a period differing that of the wave. Research by Choi and Tiron found that Crapper waves were stable to super-harmonic perturbations but unstable to sub-harmonic perturbations. It would be natural to determine if this pattern continues for gravity-capillary waves whose Bond number is greater than zero.

Another area for future research is in analyzing the stability of other types of overturned waves. For example, additional effort could prove effective in simulating the Vortex Sheet equations. If so, many additional wave profiles would be available for stability analysis.

VI. Conclusion

In an effort to determine the stability of overturned traveling waves, two methods were developed: (1) Spectral Stability Analysis (SSA) and (2) Dynamic Stability Analysis (DSA). These two methods were validated on the pendulum equation and the Akers-Milewski equation, two systems with known stabilities. The Vortex Sheet equations were considered as a system to investigate overturned traveling waves. However, complications associated with the Vortex Sheet equations led to using the conformally-mapped Euler (CME) equations. The SSA and DSA methods were successfully adapted to the CME equations. The SSA method faced the challenge of spurious eigenvalues emerging from numerical artifacts. The DSA method faced the challenge of aliasing errors. Numerical methods to overcome these challenges were successfully implemented. The DSA and SSA methods were validated by implementation on Crapper waves with known stability. The estimated eigenvalues given by SSA and DSA for gravity-capillary waves agreed in their predictions of stability. The stability of a sequence of branches of gravity-capillary waves with Bond numbers varying from 0.0 to 2.99 was investigated. Those branches of waves with a Bond number less than two were shown to be spectrally stable to super-harmonic perturbations, including the overturned waves. The branches of waves with a Bond number greater than or equal to two were shown to have amplitude ranges of instability. All of the overturned waves with Bond numbers greater than or equal to two were unstable. The SSA and DSA methods were also compared as methods in evaluating the stability of waves. The SSA method was found to be faster and to give more information about the spectrum of a wave, whereas the DSA method provides the dynamics of a wave as it evolves. Lastly, areas for future research were presented.

Appendix A. Derivation of Spectral Stability Analysis for Conformally-Mapped Euler Equations

Assume there is a steady wave, whose variables are X_0, Y_0, Ψ_0, Φ_0, and J_0. Since this is a steady wave, the time derivative of these variables is zero. Now, consider a small perturbation to each of these variables,

$$X(\xi,0) = X_0(\xi) + \delta X_1(\xi) \tag{150}$$

$$Y(\xi,0) = Y_0(\xi) + \delta Y_1(\xi) \tag{151}$$

$$\Psi(\xi,0) = \Psi_0(\xi) + \delta \Psi_1(\xi) \tag{152}$$

$$\Phi(\xi,0) = \Phi_0(\xi) + \delta \Phi_1(\xi) \tag{153}$$

$$J(\xi,0) = J_0(\xi) + \delta J_1(\xi) \tag{154}$$

where δ is a small constant, and X_1, Y_1, Ψ_1, Φ_1, and J_1 are perturbations of X, Y, Ψ, Φ, and J respectively. Now assume this system evolved in time. The perturbed variables become,

$$X(\xi,t) = X_0(\xi) + \delta e^{\lambda t} X_1(\xi) \tag{155}$$

$$Y(\xi,t) = Y_0(\xi) + \delta e^{\lambda t} Y_1(\xi) \tag{156}$$

$$\Psi(\xi,t) = \Psi_0(\xi) + \delta e^{\lambda t} \Psi_1(\xi) \tag{157}$$

$$\Phi(\xi,t) = \Phi_0(\xi) + \delta e^{\lambda t} \Phi_1(\xi) \tag{158}$$

$$J(\xi,t) = J_0(\xi) + \delta e^{\lambda t} J_1(\xi). \tag{159}$$

Using these definitions, expand the closures for X_ξ, Ψ_ξ, and J.

$$X_\xi = 1 - \mathscr{H}(Y_\xi) \tag{160}$$

$$X_{0\xi} + \delta e^{\lambda t} X_{1\xi} = 1 - \mathscr{H}(Y_{0\xi}) - \delta e^{\lambda t} \mathscr{H}(Y_{1\xi}), \tag{161}$$

$$\Psi_\xi = \mathscr{H}(\Phi_\xi) \tag{162}$$

$$\Psi_{0\xi} + \delta e^{\lambda t}\Psi_{1\xi} = \mathscr{H}(\Phi_{0\xi}) + \delta e^{\lambda t}\mathscr{H}(\Phi_{1\xi}), and \tag{163}$$

$$J = X_\xi^2 + Y_\xi^2 \tag{164}$$

$$J_0 + \delta e^{\lambda t}J_1 = \left(1 - \mathscr{H}(Y_{0\xi}) - \delta e^{\lambda t}\mathscr{H}(Y_{1\xi})\right)^2 + (Y_{0\xi} + \delta e^{\lambda t}Y_{1\xi})^2 \tag{165}$$

$$= 1 - 2\mathscr{H}(Y_{0\xi}) + \mathscr{H}(Y_{0\xi})^2 + Y_{0\xi}^2 \tag{166}$$

$$+ \delta e^{\lambda t}(-2\mathscr{H}(Y_{1\xi}) + 2\mathscr{H}(Y_{0\xi})\mathscr{H}(Y_{1\xi}) + 2Y_{0\xi}Y_{1\xi}) \tag{167}$$

$$+ O(\delta^2). \tag{168}$$

Next, use the definitions to expand the CME equations. Due to the length of the equations, start by expanding smaller groups of terms which will subsequently be combined to fill out the full equations.

$$\frac{(\Psi_\xi - cY_\xi)}{J} = \frac{\mathscr{H}(\Phi_{0\xi}) + \delta e^{\lambda t}\mathscr{H}(\Phi_{1\xi}) - cY_{0\xi} - c\delta e^{\lambda t}Y_{1\xi}}{J_0 + \delta e^{\lambda t}J_1} \tag{169}$$

$$= \frac{\mathscr{H}(\Phi_{0\xi}) - cY_{0\xi} + \delta e^{\lambda t}(\mathscr{H}(\Phi_{1\xi}) - cY_{1\xi})}{J_0} \cdot \left[\frac{1}{1 - \delta e^{\lambda t}\left(\frac{-J_1}{J_0}\right)}\right]. \tag{170}$$

Use a geometric series expansion for the bracketed terms on the right. NOTE: this technique will be used repeatedly in future equations without explanation.

$$\frac{(\Psi_\xi - cY_\xi)}{J} = \frac{\mathscr{H}(\Phi_{0\xi}) - cY_{0\xi} + \delta e^{\lambda t}(\mathscr{H}(\Phi_{1\xi}) - cY_{1\xi})}{J_0} \cdot \left[1 - \delta e^{\lambda t}\frac{J_1}{J_0} + O(\delta^2)\right] \tag{171}$$

$$= \frac{\mathscr{H}(\Phi_{0\xi}) - cY_{0\xi}}{J_0} \tag{172}$$

$$+ \delta e^{\lambda t}\left[\frac{\mathscr{H}(\Phi_{1\xi}) - cY_{1\xi}}{J_0} - \frac{J_1}{J_0^2}\left(\mathscr{H}(\Phi_{0\xi}) - cY_{0\xi}\right)\right] + O(\delta^2), \tag{173}$$

$$Y_\xi \mathscr{H}\left(\frac{\Psi_\xi - cY_\xi}{J}\right) = Y_{0\xi}\mathscr{H}\left(\frac{\mathscr{H}(\Phi_{0\xi}) - cY_{0\xi}}{J_0}\right) \tag{174}$$

$$+ \delta e^{\lambda t}\Bigg[Y_{1\xi}\mathscr{H}\left(\frac{\mathscr{H}(\Phi_{0\xi}) - cY_{0\xi}}{J_0}\right) \tag{175}$$

$$+ Y_{0\xi}\mathscr{H}\left(\frac{\mathscr{H}(\Phi_{1\xi}) - cY_{1\xi}}{J_0} - \frac{J_1}{J_0^2}(\mathscr{H}(\Phi_{0\xi}) - cY_{0\xi})\right)\Bigg] \tag{176}$$

$$+ O(\delta^2), \tag{177}$$

$$X_\xi\left(\frac{\Psi_\xi - cY_\xi}{J}\right) = (1 - \mathscr{H}(Y_{0\xi}))\left(\frac{\mathscr{H}(\Phi_{0\xi}) - cY_{0\xi}}{J_0}\right) \tag{178}$$

$$+ \delta e^{\lambda t}\Bigg[- \mathscr{H}(Y_{1\xi})\frac{\mathscr{H}(\Phi_{0\xi}) - cY_{0\xi}}{J_0} \tag{179}$$

$$+ (1 - \mathscr{H}(Y_{0\xi}))\left(\frac{\mathscr{H}(\Phi_{1\xi}) - cY_{1\xi}}{J_0} - \frac{J_1}{J_0^2}(\mathscr{H}(\Phi_{0\xi}) - cY_{0\xi})\right)\Bigg] \tag{180}$$

$$+ O(\delta^2), \tag{181}$$

$$\frac{\Phi_\xi^2 + \Psi_\xi^2}{J} = \frac{(\Phi_{0\xi} + \delta e^{\lambda t}\Phi_{1\xi})^2 + (\mathscr{H}(\Phi_{0\xi}) + \delta e^{\lambda t}\mathscr{H}(\Phi_{1\xi}))^2}{J_0 + \delta e^{\lambda t}J_1} \tag{182}$$

$$= \frac{\Phi_{0\xi}^2 + \mathscr{H}(\Phi_{0\xi})^2 + \delta e^{\lambda t}(2\Phi_{0\xi}\Phi_{1\xi} + 2\mathscr{H}(\Phi_{0\xi})\mathscr{H}(\Phi_{1\xi}))}{J_0} \tag{183}$$

$$\cdot \left[\frac{1}{1 - \delta e^{\lambda t}\left(\frac{-J_1}{J_0}\right)}\right] \tag{184}$$

$$= \frac{\Phi_{0\xi}^2 + \mathscr{H}(\Phi_{0\xi})^2 + \delta e^{\lambda t}(2\Phi_{0\xi}\Phi_{1\xi} + 2\mathscr{H}(\Phi_{0\xi})\mathscr{H}(\Phi_{1\xi}))}{J_0} \tag{185}$$

$$\cdot \left[1 - \delta e^{\lambda t}\frac{J_1}{J_0} + O(\delta^2)\right] \tag{186}$$

$$= \frac{\Phi_{0\xi}^2 + \mathscr{H}(\Phi_{0\xi})^2}{J_0} \tag{187}$$

$$+ \delta e^{\lambda t}\left[\frac{2(\Phi_{0\xi}\Phi_{1\xi} + \mathscr{H}(\Phi_{0\xi})\mathscr{H}(\Phi_{1\xi}))}{J_0} - \frac{J_1}{J_0^2}\left(\Phi_{0\xi}^2 + \mathscr{H}(\Phi_{0\xi})^2\right)\right] \tag{188}$$

$$+ O(\delta^2). \tag{189}$$

For the next group of terms let $\tilde{J} = J^{3/2}$. Therefore,

$$(\tilde{J}_0 + \delta e^{\lambda t}\tilde{J}_1) = (J_0 + \delta e^{\lambda t} J_1)^{3/2} \tag{190}$$

$$(\tilde{J}_0 + \delta e^{\lambda t}\tilde{J}_1)^2 = (J_0 + \delta e^{\lambda t} J_1)^3 \tag{191}$$

$$\tilde{J}_0^2 + \delta e^{\lambda t} 2\tilde{J}_0\tilde{J}_1 + O(\delta^2) = J_0^3 + \delta e^{\lambda t} 3J_0^2 J_1 + O(\delta^2). \tag{192}$$

Now solve for $\tilde{J}_0$ and $\tilde{J}_1$ in terms of J_0 and J_1,

$$\tilde{J}_0 = J_0^{3/2} \tag{193}$$

$$\tilde{J}_1 = 3/2 J_0^{1/2} J_1. \tag{194}$$

Now, use $\tilde{J}$ in place of $J^{3/2}$,

$$\frac{X_\xi Y_{\xi\xi} - X_{\xi\xi} Y_\xi}{\tilde{J}} = \frac{(1 - \mathscr{H}(Y_{0\xi}) - \delta e^{\lambda t}\mathscr{H}(Y_{1\xi}))(Y_{0\xi\xi} + \delta e^{\lambda t} Y_{1\xi\xi})}{\tilde{J}} \tag{195}$$

$$- \frac{(1 - \mathscr{H}(Y_{0\xi}) - \delta e^{\lambda t}\mathscr{H}(Y_{1\xi}))_\xi (Y_{0\xi} + \delta e^{\lambda t} Y_{1\xi})}{\tilde{J}} \tag{196}$$

$$= \frac{Y_{0\xi\xi} - Y_{0\xi\xi}\mathscr{H}(Y_{0\xi}) + Y_{0\xi}\mathscr{H}(Y_{0\xi})_\xi}{\tilde{J}} \tag{197}$$

$$+ \delta e^{\lambda t}\left[\frac{Y_{1\xi\xi} - Y_{1\xi\xi}\mathscr{H}(Y_{0\xi}) - Y_{0\xi\xi}\mathscr{H}(Y_{1\xi})}{\tilde{J}}\right. \tag{198}$$

$$\left. + \frac{Y_{1\xi}\mathscr{H}(Y_{0\xi})_\xi + Y_{0\xi}\mathscr{H}(Y_{1\xi})_\xi}{\tilde{J}}\right] \tag{199}$$

$$+ O(\delta^2). \tag{200}$$

For simplicity, let all of the $O(1)$ terms be replaced by S_0 and the $O(\delta)$ terms be replace by S_1,

$$\frac{X_\xi Y_{\xi\xi} - X_{\xi\xi} Y_\xi}{\tilde{J}} = \frac{S_0 + \delta e^{\lambda t} S_1}{\tilde{J}_0} \cdot \left[\frac{1}{1 - \delta e^{\lambda t} \frac{-\tilde{J}_1}{\tilde{J}_0}} \right] \tag{201}$$

$$= \frac{S_0 + \delta e^{\lambda t} S_1}{\tilde{J}_0} \cdot \left[1 - \delta e^{\lambda t} \frac{\tilde{J}_1}{\tilde{J}_0} + O(\delta^2) \right] \tag{202}$$

$$= \frac{S_0}{\tilde{J}_0} + \delta e^{\lambda t} \left[\frac{S_1}{\tilde{J}_0} - \frac{\tilde{J}_1}{\tilde{J}_0^2} S_0 \right] + O(\delta^2). \tag{203}$$

Now, substitute back in for J_0 and J_1,

$$\frac{X_\xi Y_{\xi\xi} - X_{\xi\xi} Y_\xi}{J} = \frac{S_0}{J_0^{3/2}} + \delta e^{\lambda t} \left[\frac{S_1}{J_0^{3/2}} - \frac{3/2 J_0^{1/2} J_1}{(J_0^{3/2})^2} S_0 \right] \tag{204}$$

$$= \frac{S_0}{J_0^{3/2}} + \delta e^{\lambda t} \left[\frac{S_1}{J_0^{3/2}} - \frac{3 J_1}{2 J_0^{5/2}} S_0 \right], \tag{205}$$

$$\Phi_\xi \mathscr{H} \left(\frac{\Psi_\xi - c Y_\xi}{J} \right) = \Phi_{0\xi} \mathscr{H} \left(\frac{\mathscr{H}(\Phi_{0\xi}) - c Y_{0\xi}}{J_0} \right) \tag{206}$$

$$+ \delta e^{\lambda t} \Bigg[\Phi_{1\xi} \mathscr{H} \left(\frac{\mathscr{H}(\Phi_{0\xi}) - c Y_{0\xi}}{J_0} \right) \tag{207}$$

$$+ \Phi_{0\xi} \mathscr{H} \left(\frac{\mathscr{H}(\Phi_{1\xi}) - c Y_{1\xi}}{J_0} - \frac{J_1}{J_0^2} (\mathscr{H}(\Phi_{0\xi}) - c Y_{0\xi}) \right) \Bigg] \tag{208}$$

$$+ O(\delta^2), \tag{209}$$

$$\Psi_\xi\left(\frac{(\Psi_\xi - cY_\xi)}{J}\right) = \mathscr{H}(\Phi_{0\xi})\left(\frac{\mathscr{H}(\Phi_{0\xi}) - cY_{0\xi}}{J_0}\right) \tag{210}$$

$$+ \delta e^{\lambda t}\Bigg[\mathscr{H}(\Phi_{1\xi})\left(\frac{\mathscr{H}(\Phi_{0\xi}) - cY_{0\xi}}{J_0}\right) \tag{211}$$

$$+ \mathscr{H}(\Phi_{0\xi})\left(\frac{\mathscr{H}(\Phi_{1\xi}) - cY_{1\xi}}{J_0} - \frac{J_1}{J_0^2}(\mathscr{H}(\Phi_{0\xi}) - cY_{0\xi})\right)\Bigg] \tag{212}$$

$$+ O(\delta^2), \tag{213}$$

$$\frac{X_\xi\Phi_\xi + \Psi_\xi Y_\xi}{J} = \frac{(1 - \mathscr{H}(Y_{0\xi}) - \delta e^{\lambda t}\mathscr{H}(Y_{1\xi}))(\Phi_{0\xi} + \delta e^{\lambda t}\Phi_{1\xi})}{J_0 + \delta e^{\lambda t}J_1} \tag{214}$$

$$+ \frac{(\mathscr{H}(\Phi_{0\xi}) + \delta e^{\lambda t}\mathscr{H}(\Phi_{1\xi}))(Y_{0\xi} + \delta e^{\lambda t}Y_{1\xi})}{J_0 + \delta e^{\lambda t}J_1} \tag{215}$$

$$= \left(\frac{1}{J_0}\right)\Big(\Phi_{0\xi} - \mathscr{H}(Y_{0\xi})\Phi_{0\xi} + \mathscr{H}(\Phi_{0\xi})Y \tag{216}$$

$$+ \delta e^{\lambda t}[\Phi_{1\xi} - \mathscr{H}(Y_{0\xi})\Phi_{1\xi} - \mathscr{H}(Y_{1\xi})\Phi_{0\xi} + \mathscr{H}(\Phi_{0\xi})Y_{1\xi} \tag{217}$$

$$+ \mathscr{H}(\Phi_{1\xi})Y_{0\xi}]\Big) \cdot \left[\frac{1}{1 - \delta e^{\lambda t}\frac{-J_1}{J_0}}\right] \tag{218}$$

$$+ O(\delta^2) \tag{219}$$

$$= \left(\frac{1}{J_0}\right)\Big(\Phi_{0\xi} - \mathscr{H}(Y_{0\xi})\Phi_{0\xi} + \mathscr{H}(\Phi_{0\xi})Y \tag{220}$$

$$+ \delta e^{\lambda t}[\Phi_{1\xi} - \mathscr{H}(Y_{0\xi})\Phi_{1\xi} - \mathscr{H}(Y_{1\xi})\Phi_{0\xi} + \mathscr{H}(\Phi_{0\xi})Y_{1\xi} \tag{221}$$

$$+ \mathscr{H}(\Phi_{1\xi})Y_{0\xi}]\Big) \cdot \left[1 - \delta e^{\lambda t}\frac{J_1}{J_0} + O(\delta^2)\right] \tag{222}$$

$$= \frac{\Phi_{0\xi} - \mathscr{H}(Y_{0\xi})\Phi_{0\xi} + \mathscr{H}(\Phi_{0\xi})Y_{0\xi}}{J_0} \tag{223}$$

$$+ \delta e^{\lambda t}\Bigg[\frac{\Phi_{1\xi} - \mathscr{H}(Y_{0\xi})\Phi_{1\xi} - \mathscr{H}(Y_{1\xi})\Phi_{0\xi}}{J_0} \tag{224}$$

$$+ \frac{\mathscr{H}(\Phi_{0\xi})Y_{1\xi} + \mathscr{H}(\Phi_{1\xi})Y_{0\xi}}{J_0} \tag{225}$$

$$- \frac{J_1}{J_0^2}\left(\Phi_{0\xi} - \mathscr{H}(Y_{0\xi})\Phi_{0\xi} + \mathscr{H}(\Phi_{0\xi})Y_{0\xi}\right)\Bigg] \tag{226}$$

$$+ O(\delta^2). \tag{227}$$

Now, combine all of the terms into the CME equations, converting everything into terms of Y and Φ,

$$Y_t = Y_\xi \mathscr{H}\left(\frac{\Psi_\xi - cY_\xi}{J}\right) - X_\xi\left(\frac{\Psi_\xi - cY_\xi}{J}\right) \tag{228}$$

$$Y_{0t} + \delta e^{\lambda t}\lambda Y_1 = \left[Y_{0\xi}\mathscr{H}\left(\frac{\mathscr{H}(\Phi_{0\xi}) - cY_{0\xi}}{J_0}\right)\right. \tag{229}$$

$$\left. + (1 - \mathscr{H}(Y_{0\xi}))\left(\frac{\mathscr{H}(\Phi_{0\xi}) - cY_{0\xi}}{J_0}\right)\right] \tag{230}$$

$$+ \delta e^{\lambda t}\left[Y_{1\xi}\mathscr{H}\left(\frac{\mathscr{H}(\Phi_{0\xi}) - cY_{0\xi}}{1 - 2\mathscr{H}(Y_{0\xi}) + \mathscr{H}(Y_{0\xi})^2 + Y_{0\xi}^2}\right)\right. \tag{231}$$

$$+ Y_{0\xi}\mathscr{H}\left[\frac{\mathscr{H}(\Phi_{1\xi}) - cY_{1\xi}}{1 - 2\mathscr{H}(Y_{0\xi}) + \mathscr{H}(Y_{0\xi})^2 + Y_{0\xi}^2}\right. \tag{232}$$

$$\left.\left. - \frac{-2\mathscr{H}(Y_{1\xi}) + 2\mathscr{H}(Y_{0\xi})\mathscr{H}(Y_{1\xi}) + 2Y_{0\xi}Y_{1\xi}}{(1 - 2\mathscr{H}(Y_{0\xi}) + \mathscr{H}(Y_{0\xi})^2 + Y_{0\xi}^2)^2}(\mathscr{H}(\Phi_{0\xi}) - cY_{0\xi})\right]\right. \tag{233}$$

$$- \mathscr{H}(Y_{1\xi})\frac{\mathscr{H}(\Phi_{0\xi}) - cY_{0\xi}}{1 - 2\mathscr{H}(Y_{0\xi}) + \mathscr{H}(Y_{0\xi})^2 + Y_{0\xi}^2} \tag{234}$$

$$+ (1 - \mathscr{H}(Y_{0\xi}))\left[\frac{\mathscr{H}(\Phi_{1\xi}) - cY_{1\xi}}{1 - 2\mathscr{H}(Y_{0\xi}) + \mathscr{H}(Y_{0\xi})^2 + Y_{0\xi}^2}\right. \tag{235}$$

$$\left.\left. - \frac{-2\mathscr{H}(Y_{1\xi}) + 2\mathscr{H}(Y_{0\xi})\mathscr{H}(Y_{1\xi}) + 2Y_{0\xi}Y_{1\xi}}{(1 - 2\mathscr{H}(Y_{0\xi}) + \mathscr{H}(Y_{0\xi})^2 + Y_{0\xi}^2)^2}(\mathscr{H}(\Phi_{0\xi}) - cY_{0\xi})\right]\right]. \tag{236}$$

Note that the $O(1)$ terms are associated with the steady wave. Therefore, their values are unchanged with time and can be removed. The remaining terms all have $\delta e^{\lambda t}$,

which can be canceled through the equation. The result is,

$$\lambda Y_1 = Y_{1\xi}\mathscr{H}\left(\frac{\mathscr{H}(\Phi_{0\xi}) - cY_{0\xi}}{1 - 2\mathscr{H}(Y_{0\xi}) + \mathscr{H}(Y_{0\xi})^2 + Y_{0\xi}^2}\right) \tag{237}$$

$$+ Y_{0\xi}\mathscr{H}\left[\frac{\mathscr{H}(\Phi_{1\xi}) - cY_{1\xi}}{1 - 2\mathscr{H}(Y_{0\xi}) + \mathscr{H}(Y_{0\xi})^2 + Y_{0\xi}^2}\right. \tag{238}$$

$$\left. - \frac{-2\mathscr{H}(Y_{1\xi}) + 2\mathscr{H}(Y_{0\xi})\mathscr{H}(Y_{1\xi}) + 2Y_{0\xi}Y_{1\xi}}{(1 - 2\mathscr{H}(Y_{0\xi}) + \mathscr{H}(Y_{0\xi})^2 + Y_{0\xi}^2)^2}(\mathscr{H}(\Phi_{0\xi}) - cY_{0\xi})\right] \tag{239}$$

$$- \mathscr{H}(Y_{1\xi})\frac{\mathscr{H}(\Phi_{0\xi}) - cY_{0\xi}}{1 - 2\mathscr{H}(Y_{0\xi}) + \mathscr{H}(Y_{0\xi})^2 + Y_{0\xi}^2} \tag{240}$$

$$+ (1 - \mathscr{H}(Y_{0\xi}))\left[\frac{\mathscr{H}(\Phi_{1\xi}) - cY_{1\xi}}{1 - 2\mathscr{H}(Y_{0\xi}) + \mathscr{H}(Y_{0\xi})^2 + Y_{0\xi}^2}\right. \tag{241}$$

$$\left. \left. - \frac{-2\mathscr{H}(Y_{1\xi}) + 2\mathscr{H}(Y_{0\xi})\mathscr{H}(Y_{1\xi}) + 2Y_{0\xi}Y_{1\xi}}{(1 - 2\mathscr{H}(Y_{0\xi}) + \mathscr{H}(Y_{0\xi})^2 + Y_{0\xi}^2)^2}(\mathscr{H}(\Phi_{0\xi}) - cY_{0\xi})\right]\right] \tag{242}$$

$$= G_1(Y_1, \Phi_1). \tag{243}$$

Note that G_1 is not a function of Y_0 and Φ_0 because these terms are fixed from the steady wave solution. Next, combine terms for the second CME equation. As with the previous equation, the $O(1)$ terms can be omitted and the $\delta e^{\lambda t}$ term can be cancelled.

Thus,

$$\lambda\Phi_1 = -(1/2)\Bigg[\frac{2(\Phi_{0\xi}\Phi_{1\xi} + \mathscr{H}(\Phi_{0\xi})\mathscr{H}(\Phi_{1\xi}))}{1 - 2\mathscr{H}(Y_{0\xi}) + \mathscr{H}(Y_{0\xi})^2 + Y_{0\xi}^2} \tag{244}$$

$$- \frac{-2\mathscr{H}(Y_{1\xi}) + 2\mathscr{H}(Y_{0\xi})\mathscr{H}(Y_{1\xi}) + 2Y_{0\xi}Y_{1\xi}}{(1 - 2\mathscr{H}(Y_{0\xi}) + \mathscr{H}(Y_{0\xi})^2 + Y_{0\xi}^2)^2}\left(\Phi_{0\xi}^2 + \mathscr{H}(\Phi_{0\xi})^2\right)\Bigg] \tag{245}$$

$$- BY_1 \tag{246}$$

$$+ \frac{Y_{1\xi\xi} - Y_{1\xi\xi}\mathscr{H}(Y_{0\xi}) - Y_{0\xi\xi}\mathscr{H}(Y_{1\xi}) + Y_{1\xi}\mathscr{H}(Y_{0\xi})_\xi + Y_{0\xi}\mathscr{H}(Y_{1\xi})_\xi}{(1 - 2\mathscr{H}(Y_{0\xi}) + \mathscr{H}(Y_{0\xi})^2 + Y_{0\xi}^2)^{3/2}} \tag{247}$$

$$- \left(\frac{3}{2}\right)\frac{-2\mathscr{H}(Y_{1\xi}) + 2\mathscr{H}(Y_{0\xi})\mathscr{H}(Y_{1\xi}) + 2Y_{0\xi}Y_{1\xi}}{(1 - 2\mathscr{H}(Y_{0\xi}) + \mathscr{H}(Y_{0\xi})^2 + Y_{0\xi}^2)^{5/2}}\cdot \tag{248}$$

$$(Y_{0\xi\xi} - Y_{0\xi\xi}\mathscr{H}(Y_{0\xi}) + Y_{0\xi}\mathscr{H}(Y_{0\xi})_\xi) \tag{249}$$

$$+ \Phi_{1\xi}\mathscr{H}\left(\frac{\mathscr{H}(\Phi_{0\xi}) - cY_{0\xi}}{1 - 2\mathscr{H}(Y_{0\xi}) + \mathscr{H}(Y_{0\xi})^2 + Y_{0\xi}^2}\right) \tag{250}$$

$$+ \Phi_{0\xi}\mathscr{H}\Bigg[\frac{\mathscr{H}(\Phi_{1\xi}) - cY_{1\xi}}{1 - 2\mathscr{H}(Y_{0\xi}) + \mathscr{H}(Y_{0\xi})^2 + Y_{0\xi}^2} \tag{251}$$

$$- \frac{-2\mathscr{H}(Y_{1\xi}) + 2\mathscr{H}(Y_{0\xi})\mathscr{H}(Y_{1\xi}) + 2Y_{0\xi}Y_{1\xi}}{(1 - 2\mathscr{H}(Y_{0\xi}) + \mathscr{H}(Y_{0\xi})^2 + Y_{0\xi}^2)^2}(\mathscr{H}(\Phi_{0\xi}) - cY_{0\xi})\Bigg] \tag{252}$$

$$+ \mathscr{H}(\Phi_{1\xi})\left(\frac{\mathscr{H}(\Phi_{0\xi}) - cY_{0\xi}}{1 - 2\mathscr{H}(Y_{0\xi}) + \mathscr{H}(Y_{0\xi})^2 + Y_{0\xi}^2}\right) \tag{253}$$

$$+ \mathscr{H}(\Phi_{0\xi})\Bigg[\frac{\mathscr{H}(\Phi_{1\xi}) - cY_{1\xi}}{1 - 2\mathscr{H}(Y_{0\xi}) + \mathscr{H}(Y_{0\xi})^2 + Y_{0\xi}^2} \tag{254}$$

$$- \frac{-2\mathscr{H}(Y_{1\xi}) + 2\mathscr{H}(Y_{0\xi})\mathscr{H}(Y_{1\xi}) + 2Y_{0\xi}Y_{1\xi}}{(1 - 2\mathscr{H}(Y_{0\xi}) + \mathscr{H}(Y_{0\xi})^2 + Y_{0\xi}^2)^2}(\mathscr{H}(\Phi_{0\xi}) - cY_{0\xi})\Bigg] \tag{255}$$

$$+ c\Bigg[\frac{\Phi_{1\xi} - \mathscr{H}(Y_{0\xi})\Phi_{1\xi} - \mathscr{H}(Y_{1\xi})\Phi_{0\xi}}{1 - 2\mathscr{H}(Y_{0\xi}) + \mathscr{H}(Y_{0\xi})^2 + Y_{0\xi}^2} \tag{256}$$

$$+ \frac{\mathscr{H}(\Phi_{0\xi})Y_{1\xi} + \mathscr{H}(\Phi_{1\xi})Y_{0\xi}}{1 - 2\mathscr{H}(Y_{0\xi}) + \mathscr{H}(Y_{0\xi})^2 + Y_{0\xi}^2} \tag{257}$$

$$- \frac{-2\mathscr{H}(Y_{1\xi}) + 2\mathscr{H}(Y_{0\xi})\mathscr{H}(Y_{1\xi}) + 2Y_{0\xi}Y_{1\xi}}{(1 - 2\mathscr{H}(Y_{0\xi}) + \mathscr{H}(Y_{0\xi})^2 + Y_{0\xi}^2)^2}\cdot \tag{258}$$

$$(\Phi_{0\xi} - \mathscr{H}(Y_{0\xi})\Phi_{0\xi} + \mathscr{H}(\Phi_{0\xi})Y_{0\xi})\Bigg] \tag{259}$$

$$= G_2(Y_1, \Phi_1). \tag{260}$$

Now, combine the two CME equations into a matrix representation,

$$\lambda \begin{bmatrix} Y_1 \\ \Phi_1 \end{bmatrix} = \begin{bmatrix} G1 \\ G2 \end{bmatrix} \begin{bmatrix} Y_1 \\ \Phi_1 \end{bmatrix} \tag{261}$$

$$\lambda v = \quad A \quad v \tag{262}$$

where v is a vector of the eigenvectors Y_1 and Φ_1 and matrix A can be considered an operator acting on v. This in now in the form of a general eigenvalue problem. The procedure from this point forward is identical to that which was presented in the Akers-Milewski equation. It is repeated here for completeness. The operator A is infinitely dimensional. To approximate A, change both sides of the equation into Fourier space,

$$\widehat{\lambda v} = \widehat{Av}. \tag{263}$$

Now, consider F as a linear operator that transforms a vector in normal space into a vector in Fourier space. Applying F and an identity operator to the right side of the equation gives the following result,

$$\lambda \hat{v} = FAv \tag{264}$$

$$= FAIv \tag{265}$$

$$= FAF^{-1}Fv. \tag{266}$$

Let FAF^{-1} be replaced by another linear operator, $\mathscr{A}$. Also, note that $Fv = \hat{v}$. Therefore,

$$\lambda \hat{v} = \mathscr{A}\hat{v}. \tag{267}$$

This equation is in the form of a general spectral problem. Furthermore, operator A is similar to operator $\mathscr{A}$ (i.e., they have the same spectrum). Although operator $\mathscr{A}$

is also unknown, there is a technique to determine its elements, column by column. First, note that $\widehat{Av} = \mathscr{A}\hat{v}$. Now, consider a perturbation vector, v_1, whose Fourier transform is $\hat{v}_1 = [1\ 0\ 0\ \cdots]^{\mathrm{T}} = e_1 =$ canonical basis vector for the first coordinate. Therefore, $v_1 = \mathscr{F}^{-1}(\hat{v}_1)$. Now, plugging this vector into the right hand side of Equations 243 and 260 results in Av_1. Taking the Fourier transform of this result gives $\widehat{Av_1}$. Finally, note that $\mathscr{A}\hat{v}_1 = \mathscr{A}[1\ 0\ 0\ \cdots]^{\mathrm{T}} = \mathscr{A}_1$, the first column of $\mathscr{A}$. Similarly, $\mathscr{A}\hat{v}_2 = \mathscr{A}[0\ 1\ 0\ \cdots]^{\mathrm{T}} = \mathscr{A}_2$, the second column of $\mathscr{A}$. This process is then repeated for each column of $\mathscr{A}$. This process is allowed because v_1 is a smooth function in real space. After $\mathscr{A}$ is fully determined, the eigenvalues are calculated via MATLAB's 'eig' function.

Bibliography

1. How to plot stability region of Fourier analysis. *Mathematica StackExcange*, 2014.

2. Benjamin F. Akers, David M. Ambrose, Kevin Pond, and J. Douglas Wright. Overturned internal capillary–gravity waves. *European Journal of Mechanics-B/Fluids*, 57:143–151, 2016.

3. Benjamin F. Akers, David M. Ambrose, and J. Douglas Wright. Traveling waves from the arclength parameterization: Vortex sheets with surface tension. *Interfaces and Free Boundaries*, 15(3):359–380, 2013.

4. Benjamin F. Akers, David M. Ambrose, and J. Douglas Wright. Gravity perturbed crapper waves. *Proceedings of the Royal Society A: Mathematical, Physical and Engineering Sciences*, 470(2161):20130526, 2014.

5. Benjamin F. Akers and David P. Nicholls. Traveling waves in deep water with gravity and surface tension. *SIAM Journal on Applied Mathematics*, 70(7):2373–2389, 2010.

6. Benjamin F. Akers and David P. Nicholls. Spectral stability of deep two-dimensional gravity water waves: repeated eigenvalues. *SIAM Journal on Applied Mathematics*, 72(2):689–711, 2012.

7. Benjamin F. Akers and David P. Nicholls. Spectral stability of deep two-dimensional gravity-capillary water waves. *Studies in Applied Mathematics*, 130(2):81–107, 2013.

8. Benjamin F. Akers and David P. Nicholls. The spectrum of finite depth water waves. *European Journal of Mechanics-B/Fluids*, 46:181–189, 2014.

9. Uri M. Ascher, Steven J. Ruuth, and Brian T.R. Wetton. Implicit-explicit methods for time-dependent partial differential equations. *SIAM Journal on Numerical Analysis*, 32(3):797–823, 1995.

10. T. Brooke Benjamin. Instability of periodic wavetrains in nonlinear dispersive systems. *Proceedings of the Royal Society of London. Series A. Mathematical and Physical Sciences*, 299(1456):59–76, 1967.

11. T. Brooke Benjamin and James E. Feir. The disintegration of wave trains on deep water part 1. theory. *Journal of Fluid Mechanics*, 27(3):417–430, 1967.

12. William E. Boyce and Richard C. DiPrima. *Elementary Differential Equations and Boundary Value Problems, 8th Edition*. John Wiley & Sons, 2005.

13. William E. Boyce and Richard C. DiPrima. *Elementary Differential Equations and Boundary Value Problems, 8th Edition*. John Wiley & Sons, 2005.

14. William E. Boyce and Richard C. DiPrima. *Elementary Differential Equations and Boundary Value Problems, 8th Edition*. John Wiley & Sons, 2005.

15. A. Cauchy and S. Poisson. Memoire sur la theorie des ondes, mem. *De l'acad. roy. des Science, i*, 1816.

16. Augustin Louis Baron Cauchy. *Théorie de la propagation des ondes à la surface d'un fluide pesant d'une profondeur indéfinie*. Académie Royale des Sciences, 1816.

17. Héctor Ceniceros and Thomas Hou. Convergence of a non-stiff boundary integral method for interfacial flows with surface tension. *Mathematics of Computation*, 67(221):137–182, 1998.

18. B. Chen and P.G. Saffman. Three-dimensional stability and bifurcation of capillary and gravity waves on deep water. *Studies in Applied Mathematics*, 72(2):125–147, 1985.

19. Alex D.D. Craik. The origins of water wave theory. *Annual review of fluid mechanics*, 36, 2004.

20. Alex D.D. Craik. George Gabriel Stokes on water wave theory. *Annu. Rev. Fluid Mech.*, 37:23–42, 2005.

21. G.D. Crapper. An exact solution for progressive capillary waves of arbitrary amplitude. *Journal of Fluid Mechanics*, 2(6):532–540, 1957.

22. Pierre Simon de Laplace. Suite des recherches sur plusieurs points du systeme du monde (xxv–xxvii). mém. présentés acad. r. *Sci. Inst. France*, pages 542–552, 1776.

23. T. Dean, S. Leach, and H. Shatkay. Introduction to learning dynamical systems. *Brown University*, 2020.

24. Bernard Deconinck and J. Nathan Kutz. Computing spectra of linear operators using the floquet–fourier–hill method. *Journal of Computational Physics*, 219(1):296–321, 2006.

25. Bernard Deconinck and Katie Oliveras. The instability of periodic surface gravity waves. *Journal of fluid mechanics*, 675:141–167, 2011.

26. Frédéric Dias and Christian Kharif. Nonlinear gravity and capillary-gravity waves. *Annual review of fluid mechanics*, 31(1):301–346, 1999.

27. Leonhard Euler. Continuation des recherches sur la théorie du mouvement des fluides. *Mémoires de l'académie des sciences de Berlin*, pages 316–361, 1757.

28. Leonhard Euler. Principes généraux du mouvement des fluides. *Mémoires de l'Académie des Sciences de Berlin*, pages 274–315, 1757.

29. Leonhard Euler. Principia motus fluidorum. *Novi commentarii academiae scientiarum Petropolitanae*, pages 271–311, 1761.

30. Etienne Forest and Ronald D Ruth. Fourth-order symplectic integration. *Physica D: Nonlinear Phenomena*, 43(1):105–117, 1990.

31. Marc Francius and Christian Kharif. Three-dimensional instabilities of periodic gravity waves in shallow water. *Journal of Fluid Mechanics*, 561:417–437, 2006.

32. S.J. Hogan. The superharmonic normal mode instabilities of nonlinear deep-water capillary waves. *Journal of Fluid Mechanics*, 190:165–177, 1988.

33. Thomas Y. Hou, John S. Lowengrub, and Michael J. Shelley. Removing the stiffness from interfacial flows with surface tension. *Journal of Computational Physics*, 114(2):312–338, 1994.

34. Thomas Y. Hou, John S. Lowengrub, and Michael J. Shelley. The long-time motion of vortex sheets with surface tension. *Physics of Fluids*, 9(7):1933–1954, 1997.

35. Mathias Johansson. The Hilbert Transform. *Mathematics Master's Thesis. Växjö University, Suecia. Disponible en internet: http://w3. msi. vxu. se/exarb/mj_ex. pdf, consultado el*, 19, 1999.

36. Aly-Khan Kassam and Lloyd N. Trefethen. Fourth-order time-stepping for stiff PDEs. *SIAM Journal on Scientific Computing*, 26(4):1214–1233, 2005.

37. Christian Kharif and Alfred Ramamonjiarisoa. On the stability of gravity waves on deep water. *Journal of Fluid Mechanics*, 218:163–170, 1990.

38. Joseph Louis Lagrange. Sur la manière de rectifier deux endroits des principes de newton relatifs à la propagation du son et au mouvement des ondes. *Nouv. Mém. Acad. Berlin*, 5:591–609, 1786.

39. Michael Selwyn Longuet-Higgins. The instabilities of gravity waves of finite amplitude in deep water i. superharmonics. *Proceedings of the Royal Society of London. A. Mathematical and Physical Sciences*, 360(1703):471–488, 1978.

40. Michael Selwyn Longuet-Higgins. The instabilities of gravity waves of finite amplitude in deep water ii. subharmonics. *Proceedings of the Royal Society of London. A. Mathematical and Physical Sciences*, 360(1704):489–505, 1978.

41. D.I. Meiron and P.G. Saffman. Overhanging interfacial gravity waves of large amplitude. *Journal of Fluid Mechanics*, 129:213–218, 1983.

42. Paul A. Milewski, J-M Vanden-Broeck, and Zhan Wang. Dynamics of steep two-dimensional gravity–capillary solitary waves. *Journal of Fluid Mechanics*, 664:466–477, 2010.

43. Isaac Newton. *Philosophiae naturalis principia mathematica*, volume 2. Apud Guil. and Joh. Innys, Regiæ Societatis typographos, 1726.

44. Hisashi Okamoto et al. *The mathematical theory of permanent progressive water-waves*, volume 20. World Scientific, 2001.

45. John Scott Russell. *Report on Waves: Made to the Meetings of the British Association in 1842-43*. 1845.

46. George Gabriel Stokes. On the theory of oscillatory waves, volume 1 of cambridge library collection-mathematics, 1847.

47. Roxana Tiron and Wooyoung Choi. Linear stability of finite-amplitude capillary waves on water of infinite depth. *Journal of fluid mechanics*, 696:402–422, 2012.

REPORT DOCUMENTATION PAGE

Form Approved
OMB No. 0704–0188

1. REPORT DATE *(DD–MM–YYYY)*	2. REPORT TYPE	3. DATES COVERED *(From — To)*
08–04–2021	PhD Dissertation	Jul 2019 — Aug 2021

4. TITLE AND SUBTITLE

INSTABILITIES OF OVERTURNED TRAVELING WAVES

5a. CONTRACT NUMBER

5b. GRANT NUMBER

5c. PROGRAM ELEMENT NUMBER

6. AUTHOR(S)

Tyler B. Pierce

5d. PROJECT NUMBER

5e. TASK NUMBER

5f. WORK UNIT NUMBER

7. PERFORMING ORGANIZATION NAME(S) AND ADDRESS(ES)

Air Force Institute of Technology
Graduate School of Engineering and Management (AFIT/EN)
2950 Hobson Way
WPAFB OH 45433-7765

8. PERFORMING ORGANIZATION REPORT NUMBER

AFIT/ENC/DS/21-S-002

9. SPONSORING / MONITORING AGENCY NAME(S) AND ADDRESS(ES)

Department of Mathematics and Statistics
2950 Hobson Way
WPAFB OH 45433-7765
Email: tyler.pierce@afit.edu

10. SPONSOR/MONITOR'S ACRONYM(S)

AFIT/ENC

11. SPONSOR/MONITOR'S REPORT NUMBER(S)

12. DISTRIBUTION / AVAILABILITY STATEMENT

DISTRIBUTION STATEMENT A:
APPROVED FOR PUBLIC RELEASE; DISTRIBUTION UNLIMITED.

13. SUPPLEMENTARY NOTES

14. ABSTRACT

The instabilities of overturned traveling waves are determined by the use of spectral methods. Two separate numerical methods, Spectral Stability Analysis and Dynamic Stability Analysis, are used to assess the instabilities of branches of waves solved from conformally-mapped Euler equations. The branches of waves with Bond number less than two were found to be spectrally stable to super-harmonic perturbations. The branches of waves with Bond number in [2,3) had some waves that were stable and some that were unstable. All overturned waves with Bond number greater than or equal to two were unstable.

15. SUBJECT TERMS

Stability, Overturned Waves, Spectral Stability, Water Waves

16. SECURITY CLASSIFICATION OF:			17. LIMITATION OF ABSTRACT	18. NUMBER OF PAGES	19a. NAME OF RESPONSIBLE PERSON
a. REPORT	b. ABSTRACT	c. THIS PAGE			Dr. Benjamin Akers, AFIT/ENC
U	U	U	U	101	19b. TELEPHONE NUMBER *(include area code)* (937) 255-3636; benjamin.akers@afit.edu